Experimental Elasticity of Earth's Deep Mantle

Hauke Marquardt[1], Andrew R. Thomson[2]

[1]*Department of Earth Sciences, University of Oxford, Oxford, OX1 3QR, UK*
[2]*Department of Earth Sciences, University College London, London, WC1E 6BT, UK*

Abstract (200 words):
Remote sensing by seismology provides increasingly detailed views on the seismic wave velocity structure of Earth's deep mantle. The interpretation of these observations critically relies on quantitative knowledge of the elastic properties of Earth's mantle minerals. This knowledge comes largely from experimental *in-situ* measurements of sound wave velocities of mantle minerals at high-pressure/-temperature, a field that has significantly evolved within the past decade. In this Technical Review, we highlight the major methodologies employed and discuss their advantages, limitations and future potential. We focus on light scattering techniques in the diamond-anvil cell and ultrasonic methods in large volume presses since these techniques have provided – and likely will provide – the majority of elasticity data on deep mantle minerals in the foreseeable future. We summarize the current state of knowledge with respect to the elastic properties of the minerals making up the transition zone and lower mantle, where substantial advances have been recently made, and highlight major gaps in published data.

1. Introduction

Physical, chemical and geodynamic properties and processes occurring throughout the Earth's mantle govern the behaviour of our planet's interior, and in turn exert strong controls on the nature of surface plate tectonics. Thus, to successfully model the evolution of Earth, or indeed other planets, on billion-year timescales we must have an accurate and quantitative understanding of the physical and chemical properties of the planet's mantle. The major challenge with understanding the deep Earth has been, and always will remain, the lack of any direct access. Thus, it has been information from remote sensing, largely seismological observations, that has driven some of the most significant insights into our planet's deep, and otherwise hidden, interior over the last decades. Whether analysing receiver functions, precursor arrivals, or reporting tomographic models or maps of mantle anisotropy, the quantity and quality of seismological observations of Earth's interior are continuously growing at an ever-increasing pace. Indeed, the number of high-quality observations has risen to such an extent that arguably the current challenge is not a lack of observations of Earth's deep mantle, but rather their interpretation. Figure 1 shows an illustrative summary of the range of mantle seismic observations that still need to be fully understood, including the large low shear velocity provinces, velocity anomalies in the transition zone velocity and pervasive scatterers throughout the mid-mantle.

Successful inversion of seismic observations requires knowledge of the physical properties of all possible Earth materials, at any and all conditions that occur throughout the mantle. To a first-order approximation, the seismic wave velocities in any material (which are responsible for the observations seismologists can make) are governed by a few key isotropic elastic properties; the bulk modulus (K), shear modulus (G), and density (ρ) (Box 1). In the Earth's mantle, the materials in question are rock assemblages which themselves are composed from a handful of mineral species (Fig. 2). Thus, knowledge of a few elastic parameters for this handful of mineral species ought to be enough to allow full inversion of global seismological data. However, the elastic properties of each constituent phase change substantially as a function of pressure (P), temperature (T), and chemical composition (X). Consequently, whilst it has been decades since researchers first attempted to utilise seismic inversions, success has continued to seem evasive due to the lack of knowledge of elastic properties of mantle constituents in appropriate parameter space. Even the elastic properties of olivine, which is the most abundant and most heavily studied upper mantle mineral, have only been measured at temperatures up to 1300 K at pressures below 13 GPa[4]. These data are several hundred degrees below the mantle geotherm, and require significant extrapolation to directly interpret seismic observations. Data for other mantle phases are even more sparse, normally limited to low pressure and/or

54   temperature and very few constrain elastic anisotropy at all. Thus, reliable seismic inversions remain a
55   "dream". It is only with the advent of new in-situ techniques over the last few years that measurements of
56   minerals' elasticity at pressure and/or temperature conditions approaching those relevant for the mantle[5-17]
57   have become widely possible. These developments now provide increased hope that the long-realised
58   potential of the elasticity-based approach to understanding the Earth's interior may begin to flourish.

60   However, recent steps forward have also revealed additional hurdles. The emerging consensus is that the
61   interpretation of seismic observations is far more complicated than previously assumed, with other changes
62   in mineral properties (in addition to changes in *P*, *T* and *X*) known to affect, or even dominate, seismic
63   velocities. These extra degrees of freedom range from the spin state of valence elements to the presence
64   and concentration of defects and the oxygen fugacity. Some of these processes are summarised in Fig. 2. As
65   a result, the traditional interpretation of seismic tomography, which assigns velocity variations to changes in
66   temperature, might not always be sufficient to explain the origin of the variations observed. While the
67   traditional interpretation likely holds in some localities, it might completely fail in others. One potential
68   example are regions where ferropericlase may undergo its iron spin transition[19]. Here, compressional wave
69   velocities are theorised to increase with temperature – not decrease as traditionally expected[16,20,21] (Fig. 2b).
70   This is just one of several hypotheses that is awaiting verification from high-*PT* elasticity measurements.
71   Importantly, since many of the predicted mineralogical changes occur over extended depth ranges (Fig. 2a),
72   established equation of state (EoS) extrapolations[22] that have been the backbone of any mineral physics
73   based interpretations for decades will fail as they cannot easily replicate these non-linear mineral properties.
74   Recent studies have made it clear that more and better measurements of elastic parameters are required.
75   Specifically, these measurements must provide improved *PT*-resolution that will allow compilation of a more
76   complete database that minimises the need to inter- and extrapolate elastic properties.

78   In this Technical Review we provide the perspective of two experimentalists on the major techniques
79   currently being used to determine elastic properties at deep mantle conditions. We summarise current
80   knowledge and highlight some of the major gaps that exist in experiments and studied materials relevant to
81   the transition zone (TZ) and lower mantle (LM). We particularly discuss the techniques employed in light of
82   their potential, their limitations and their uncertainties, and hope that this will provide a reference piece that
83   is accessible for a variety of researchers.

85   **2. Measurement techniques**
86   In principal, seismic wave velocities can be determined either by measuring them (or their related elastic
87   moduli) using experiments, or by calculating them with atomistic theory. Whilst we focus almost entirely on
88   methods for the experimental determination of velocities here, it is clear that computational methods
89   provide a complementary approach[e.g.23]. Computational techniques can range from classical mechanics to
90   molecular dynamics to full ab-initio. They can already predict the elastic properties of mantle phases with
91   uncertainties smaller than 2-5 % across the entire range of mantle *PT*-conditions and are continually evolving.
92   However, although these computational uncertainties may seem small in an absolute sense, they remain
93   sufficiently large compared with the seismic anomalies observed in the mantle. These discrepancies derive
94   from the approximations required in calculations, and the only way of significantly improving them is via
95   iteration using accurate experimental measurements as the benchmark.

97   Experimental techniques that study elastic properties of deep Earth materials are numerous (see also refs.
98   [24,25]), and include a range of X-ray inelastic scattering, (visible) light inelastic scattering and ultrasonic
99   techniques. Some of these techniques that can provide accurate and insightful data, not only for mineral
100 velocities but also elastic anisotropy, phonon density of states (PDOS), phonon lifetimes etc. are limited to
101 ambient pressures, e.g. Resonant Ultrasound Spectroscopy, RUS[26,27], or require sufficiently large samples that
102 their application at high pressure is impractical, e.g. Inelastic Neutron Scattering, INS[28]. However, many
103 others can principally be applied to study the properties of Earth materials at mantle pressures.

105 Both Inelastic X-ray Scattering[29,30] (IXS) and Nuclear Resonant Inelastic X-ray scattering[31] (NRIXS) utilise X-
106 rays to probe the phonon properties of crystalline materials, which can be related to their elastic

107 properties. Both techniques, exploiting the high-intensity and fine focus of synchrotron X-ray sources, can
108 be applied in the diamond anvil cell (DAC) at lower mantle pressures. Whilst this makes them well-suited
109 for investigating mineral properties at mantle pressures they rely on X-ray scattering ability of the sample;
110 samples composed of relatively heavy atoms, in geological terms, are the most ideal. IXS provides
111 measurements of individual points on the (linear part of the) phonon dispersion curve, from which
112 compressional and shear wave velocities can be derived[12], and can therefore give a direct constraint of
113 geophysically relevant velocities. NRIXS, on the other hand, allows determination of the partial PDOS, which
114 can directly constrain the Debye velocity (v_D)[32]. The Debye velocity, however, is not a geophysical property
115 and indirect estimates for v_p and v_s must be extracted from v_D using an averaging scheme applied alongside
116 independent constraints on the bulk modulus. Both techniques are "slow" when studying high-pressure
117 samples in a DAC, where individual velocity measurements take several hours. These time constraints,
118 partially arising from the poor X-ray scattering of silicate samples, combined with the need for dedicated
119 synchrotron facilities explains the small number of studies applying these techniques to mantle
120 minerals[12,32-37].
121
122 Brillouin Spectroscopy (BS) and Impulsive stimulated light scattering (ISLS) are light scattering techniques
123 that utilise the inelastic interactions of coherent laser sources and sample phonons, and thus do not require
124 synchrotron sources. These light scattering techniques, provide direct measurements of v_p and v_s, and due
125 to their ability to be performed in university laboratories around the world have become widespread in
126 Earth Science applications (see section 3).
127
128 Ultrasonic techniques do not exploit inelastic interactions, but instead study the elasticity of deep Earth
129 materials at high pressure by literally sending "seismic waves", albeit at extremely high-frequency (kHz-GHz
130 acoustic waves), into high-pressure samples. Techniques are based on interferometry, and can be performed
131 using either piezoelectric materials or laser sources to generate the acoustic waves. Techniques using
132 piezoelectric transducers typically operate at MHz-GHz frequencies, and are employed in conjunction with
133 the large-volume press (LVP) or DAC to directly measure v_p and v_s. Whilst both devices have been used to
134 study the acoustic velocities of mantle silicate minerals, the DAC-based GHz-ultrasonics technique has, until
135 now, been limited to ~ 10 GPa[38,39] and temperatures of only a few hundred degrees[40]. LVP-based ultrasonics
136 can be readily applied at conditions > 20 GPa and 2000K[41] (section 3).
137 Laser-based ultrasonic interferometry, which is commonly named picosecond ultrasonics (PSU), is an
138 ultrafast pulse-probe optical technique[42]. Stress waves are generated by interaction of the pulse laser with
139 the sample surface, and their arrival at the near (after reflection) or far side is detected using laser-based
140 interferometry. As PSU measurements can be performed in the DAC[42], achieving high-pressure is relatively
141 straightforward. PSU is mostly limited to opaque materials, and if transparent samples (including silicates)
142 are studied experiments are essentially analogous to time-domain Brillouin Scattering[43]. Applications of PSU
143 have so far been restricted to relatively low temperatures, but extension to mantle temperatures appears
144 possible[44].
145
146 Whilst the experimental toolbox available for studying mineral elasticity is clearly diverse, Brillouin Scattering
147 in DACs and Ultrasonic Interferometry in the LVP (Fig. 3) have, until now, provided the majority of
148 experimental elasticity data for mantle silicates. Additionally, their widespread development means they also
149 provide the best hope for expanding these datasets further in the near future. We therefore provide more
150 extensive overviews of these two techniques in the subsequent sections, deliberately highlighting their
151 limitations and current application in Earth Science research. Additionally, we also briefly outline the use of
152 X-ray diffraction on mantle minerals, because whilst it does not directly constrain velocities, it does play a
153 central role in the determination of the compressibility of mantle minerals and their high-*PT* densities. The
154 other techniques that we have briefly mentioned above might become more widely applied to deep mantle
155 minerals in the future, but have so-far mostly been used to study materials that may be present in the Earth's
156 core. Table 1 provides a summary of references to datasets for deep Earth minerals produced using each of
157 these techniques.
158
159

3. Laser light scattering techniques

3.1. Brillouin Spectroscopy

Brillouin Spectroscopy (BS) is an experimental technique capable of measuring mineral elasticity in the diamond anvil cell (DAC). Its use has become far more widespread in recent years; the number of high-pressure Brillouin Scattering systems actively used for Earth Science research has increased from 3 systems in 2000 to > 10 systems in 2020. A comprehensive discussion of the BS methodology can be found in ref. [2].

BS works by measuring a frequency shift between a probing laser and scattered light from the sample, which is generated during inelastic interactions with sound waves (acoustic phonons) in the studied material. High-pressure BS experiments on Earth mantle minerals are almost exclusively conducted in the symmetric platelet forward scattering geometry (Fig. 3a), where a direct relation exists between the measured frequency shift and the sound wave velocities[45] (Fig. 3b). These measurements require a double-side polished and transparent sample, where all sample and diamond interfaces are parallel. Sound wave velocities at high pressure can be measured with an accuracy and precision better than 1% and 0.5%, respectively, in the DAC[2,46]. Larger errors can be introduced if the scattering geometry deviates from the ideal case[46], which can be evaluated by collecting data over a large angular range[5], however this is not common practice in individual studies. BS can be performed on both single crystal samples and polycrystalline aggregates. The Brillouin signal is strongly dependent on the thickness of the sample. In experiments aimed at deep mantle pressures, samples have to be very thin (<15 μm), this leads to signal collection times of serval tenths of minutes to hours.

In single-crystal BS experiments, which constrain the full elastic tensor (Box 2), sound velocities are measured along several different propagation directions in the crystal. Subsequently, the entire data set is inverted to derive the elastic constants, from which values for the elastic moduli K and G can be calculated using appropriate averaging schemes (Box 2). Datasets often contain tens or hundreds of individual measurements, which, when inverted, provide well-constrained elastic properties. Elastic constants can principally be determined with an uncertainty < 1% (refs. [2,47]). As a generalisation, it is expected that the larger the number of measured velocities, the smaller the uncertainties in the derived constants. However, actual uncertainties depend on numerous factors including the data analysis strategy[48,49].

The price of low uncertainties, however, is time; even cubic-symmetry crystals, such as ringwoodite, majoritic garnet, ferropericlase, where measurements are only required in one plane, require very long experimental times. The situation is compounded for minerals with lower crystallographic symmetries, including orthorhombic wadsleyite and bridgmanite, which require measurements from multiple orientated samples to provide access to additional lattice directions. Recent developments have focused on facilitating the loading of multiple crystals into one diamond anvil cell[5,13,50-52]. This allows constraint of the entire elastic tensor of low symmetry crystals in a single experiment[5,50,51] or direct constraint of the effect of chemical variations on velocities[13].

It is now possible to perform single-crystal Brillouin measurements to almost 100 GPa[16,53]. But the large time requirements, often weeks for one pressure point, have mostly limited experiments to minerals with cubic symmetry; majoritic garnets[54-56], ringwoodite[13,57,58] and ferropericlase[16,17,53,59]. Only few data sets have been measured on wadsleyite[50,60-63] and bridgmanite[5,9], which are orthorhombic. Single-crystal BS measurements on CaSiO$_3$ perovskite, post-perovskite or seifertite are not possible, since none of these phases can be recovered from the high-PT synthesis. A major limitation of all BS experiments is that at pressures beyond ~ 40 GPa the measurement of compressional velocities becomes challenging. This is because the v_p signal is obscured by a peak from the diamond anvils (Fig. 3b), which occurs above ~ 20-40 GPa at room temperature for typical mantle minerals[5].

Single-crystal results at high PT using resistive-heated DACs on TZ and LM minerals are so-far limited to temperatures < 1000K, and have only been reported for ringwoodite[13,64], majoritic garnet[55], and (ferro-)periclase[65,66]. To-date, measurements using resistive-heated DACs are, therefore, not directly applicable to

mantle *PT* conditions. The use of laser-heating can possibly overcome the current obstacles in achieving mantle temperatures. However, Brillouin spectroscopy measurements demand optically transparent samples, which commonly do not absorb infrared wavelengths (~ 1μm) most widely used for laser-heating. A common solution is to add a laser-absorbing material, such as platinum to the sample. This, however, is not possible in combination with Brillouin spectroscopy as samples need to remain transparent. An alternative solution is to use CO_2 lasers that operate at wavelengths of ~10 μm to heat the sample. The longer wavelength, and absence of fibre CO_2 lasers has, however, complicated the experimental setup as they are noticeably more difficult to handle, guide and focus. We note that the recent development of wave-guide-based CO_2 lasers might improve the situation[67,68]. To-date, first single-crystal Brillouin scattering experiments have been successfully performed with laser-heating at more realistic mantle temperatures[4,68-71], but no complete data set has yet been published for any TZ or LM mineral.

Brillouin Spectroscopy experiments can also be performed on polycrystalline aggregates, which provide direct constraints on the average elastic bulk and shear moduli if the density of the sample is known (see Box 1). Measurements can be performed on pre-synthesised samples, or on those synthesised *in-situ*. Generally, measurements on polycrystalline aggregates are "easier" as compared to those on single crystals, because no directional dependence of velocities is expected. This significantly reduces the number of measurements required making polycrystalline experiments much faster.

Time gains in polycrystalline experiments do come at the expense of information on the elastic tensor and elastic anisotropy. Measured polycrystalline velocities fall somewhere in the spectrum of average velocities, and it is not straightforward to know what kind of average they represent (see Box 2). Further considerations for polycrystalline data include that apparent velocities are sensitive to samples' microstructures, such as grain size[72], the shape of grains, and/or a shape preferred orientation. Measured velocities can further be affected by lattice preferred orientations if the materials are elastically anisotropic[73]. Such elastic anisotropy might also lead to inhomogeneous stress distributions in the sample that can affect the elastic response and wave propagation[2,74]. A final consideration is that the strength of the Brillouin signal is a function of the coupling efficiency between the probing laser and the propagation direction of the acoustic phonons[e.g.75], which implies that the measured velocities could be weighted towards certain propagation directions. Whilst this is negligible for mantle minerals with low elastic anisotropy, it can significantly bias results in cases with significant anisotropy. Proof-of-concept work, comparing polycrystalline and single-crystal BS, has been reported for bridgmanite at room pressure[76], but no systematic high-pressure studies have yet been performed.

Despite the above limitations, the major advantages of polycrystalline BS are, as already mentioned, the significantly reduced experimental times which facilitates high-*T* experiments, and the possibility of measuring samples not available as single-crystals[e.g. 77]. These advantages have driven several studies; measurements have now been reported for bridgmanite[6,15,78,79], majoritic garnets[80], ferropericlase[6], (post-)stishovite[81], calcium perovskite[82] and post-perovskite[77]. Moreover, high-pressure Brillouin spectroscopy measurements on laser-heated polycrystalline aggregates of Al-bearing $MgSiO_3$ bridgmanite and MgO have been successfully performed at a temperature of 2700 K[6].

3.2. Impulsive Stimulated Light Scattering

Impulsive Stimulated Light Scattering (ISLS)[83] is a similar technique to BS, but there is no diamond interference as in BS. The major difference is that a second (pulsed) laser is used to induce the acoustic waves in the sample, and it is these induced sound waves that are measured, whereas sound waves in BS are of purely thermal origin. In almost all aspects ISLS has the same advantages and limitations of BS. The most significant differences are that ISLS is capable of measuring opaque samples as well as constraining compressional wave velocities at all pressures. However, ISLS does not provide a comparably reliable measurement of bulk shear wave velocities; these have to be inferred from an interfacial wave travelling between the sample and the pressure-transmitting medium[8]. An additional unique complication in ISLS measurements in the DAC is that the pulsed laser used to excite the acoustic waves (1064 nm wavelength) can potentially damage the diamond anvils, in particular when they contain defects and/or are strained[53].So

far, only ferropericlase and bridgmanite have been measured by ISLS at lower mantle pressures[8,9,15], with ISLS otherwise largely employed to study materials of Earth's core. A recent exciting development is the combined use of BS (to measure shear wave velocities) and ISLS (to measure compressional wave velocities) to reliably determine the velocities of bridgmanite and ferropericlase[9,53,15].

4. Ultrasonic techniques

Ultrasonic interferometry (US), most regularly performed in the large volume press (LVP), is an alternative technique for the measurement of mineral elasticity at high pressures (Fig. 3c). The principal is to pass sound pulses into a sample and detect returning echoes. By measuring the time-delay (Δt) between echoes returning from the upper and lower sample surfaces (R_2 and R_3 in Fig. 3c), and assuming the sample behaves like an infinite thin parallel plate of thickness (L), the velocity (v) of sound travelling through the sample is simply $2L/\Delta t$. Conceptually this approach is simple. In reality the high-pressure environment (either the LVP or DAC) complicates the measurements by enforcing strict geometrical constraints on, and the inability to visually see, the sample's length. Despite challenges, a well-tested and fairly standardised approach, summarised briefly here, is now used around the world such that simultaneous v_p and v_s measurements with uncertainties at the 1% level or better are possible in the LVP[14,41,84-87] or DAC[39]. Up until now the DAC-based approach has been limited to low temperature and pressure conditions of < 10 GPa, which are the limit of the silica aerosol gel that provides an acoustic bond in the DAC[38,39]. Thus, the discussion below focusses on LVP-based ultrasonic experiments (mostly performed in the multi-anvil), because at the present time this approach can actually achieve conditions of the transition zone and/or lower mantle. If future innovations extend the DAC technique beyond 10 GPa, all descriptions given here can be applied to this DAC-based ultrasonic approach, only samples are significantly smaller (< 50 μm thick) and probing frequencies higher (250+ MHz).

4.1. Large Volume Press Ultrasonic Interferometry

The most stringent constraints for LVP-US experiments are those placed on the sample. Polycrystalline samples must be parallel-faced media, that are free from porosity, cracks or any other macroscopic defects, whilst remaining fine-grained and not possessing lattice preferred orientation. Single crystals can also be measured, although to date such studies remain fairly limited in the LVP[88], likely due to difficulties associated with producing high-quality samples of sufficient size. Single crystal studies of high-pressure phases, although at < 10 GPa, have more commonly been performed using US in the DAC[39,89]. Whether poly- or monocrystalline, the sample's surfaces must be flat, and its aspect ratio should be such that its length is smaller than its radius to avoid edge effects affecting wave propagation. In practice these requirements mean that samples are usually pre-synthesised (normally by pre-sintering) and manipulated into cylinders of appropriate dimensions; for studies at > 20 GPa samples will be smaller than 2mm in diameter. Provided compression proceeds as expected and the parallel-faced sample geometry is maintained, high-quality velocity measurements are possible. The combined time requirement for one synthesis and ultrasonic experiment, including all preparation, is around 1 week; this is one of the largest downsides of this approach. A few recent studies have successfully avoided pre-synthesising samples[7,11], instead combining synthesis and ultrasonic measurements in one experiment. Whilst this approach sounds attractive, approximately halving the time requirement per ultrasonic experiment, these studies discarded data from a significant number of experimental runs due to imperfect sample geometry at target conditions (pers. comm. Thomson and Gréaux) so are not significantly more economical.

Once at high-PT conditions two measurements are required; (i) the time delay between returning echoes (Δt) and, (ii) the sample length (L). The former is more trivial. Sound pulses, with a wavelength in the sample of < $L/2$, are generated by a dual mode $LiNbO_3$ or other suitable piezoelectric transducer (e.g. ZnO is used in DAC-based US experiments[38,39]) and passed into the sample. Typical frequencies used in LVP experiments are 20-80 MHz. Returning echoes, with or without amplification, are measured using an oscilloscope (Fig. 3d). The time delay between these echoes can be determined with an uncertainty << 0.5% (normally < 0.1%). The main difficulty occurs if samples shorten sufficiently at high pressure, such that the two echoes interfere with one-another, this requires more complex signal processing. Compared with travel time measurements, the accurate determination of sample length is more challenging. In laboratory experiments, the inability to

319   directly image the sample means that the sample length can only be estimated; normally using "the Cook
320   Method" (ref. [90]). Whilst the accuracy of this approach depends on the material being studied (as it relies on
321   an equation of state for the sample), uncertainties will typically be > 3-5%. These directly translate into
322   uncertainties of 3-5% in derived sound wave velocities.
323
324   A more reliable way to quantify the sample length is by measuring it using synchrotron X-rays that penetrate
325   through the sample environment sufficiently to allow radiographic imaging of the sample[86]. By positioning
326   the cylindrical axis of the sample perpendicular to the X-ray beam, sample lengths can be determined to 1-2
327   µm precision. This typically corresponds to uncertainties in length measurements of ~ 0.2-0.4% (ref. [86]).
328   However, it remains difficult to ascertain if samples are truly cylindrical, or if they have "barrelled" during
329   compression, which might affect velocity propagation. Thus, it is reasonable to assume that combined
330   geometrical and travel time errors combine to overall uncertainties of 0.25 - 0.5% in best-case conditions for
331   synchrotron-based experiments. At synchrotron sources, density is additionally determined using X-ray
332   diffraction (see below), allowing for direct determination of K_s and G (see Box 1 for relationship with v_p and
333   v_s). The limitations of synchrotron-based ultrasonic experiments are mostly logistical and financial.
334   Synchrotron experiments require access to beamline instruments, restricted via competitive proposal
335   systems. Experimental time allocations are infrequent, typically a few days twice a year, permitting few
336   repeated measurements. Combined with individual experiment success rates of ~75%, these time and
337   financial restrictions mean that experimental datasets from LVP-ultrasonics produced at synchrotron sources
338   are sparse, and will likely remain sparse for some time.
339
340   However, huge advances have been made over the last few years, and are still ongoing. The routinely
341   accessible range of PT conditions achievable using the LVP is ever expanding (Figure 4) due to the advent of
342   new commercial tungsten carbide and sintered diamond anvil materials[91,92]. LVP-based ultrasonic
343   experiments have now been performed at conditions of ~ 27 GPa (ref. [93]) and 2400 K (ref. [94]), and there is no
344   reason to believe this field will not continue to expand. Additionally, the time required for individual
345   ultrasonic measurements has reduced from > 5 minutes to < 10 seconds[87] as oscilloscope performance has
346   rapidly improved. Up until now the LVP ultrasonic approach has predominantly been used to study
347   polycrystalline solids and their isotropic bulk properties, but recently there has been early success employing
348   it to measure the thermoplastic properties and compressional wave velocity of liquids and other amorphous
349   materials[94]. With further developments there is no obvious reason, aside from time constraints and sample
350   synthesis, why single crystals could not also be targeted more frequently in future studies, following
351   approaches used in Brillouin Spectroscopy of studying oriented single crystal samples. To our knowledge,
352   such measurements are currently limited to a single study of MgO to 8 GPa and 1600 K[88], but future work
353   could aim to constrain anisotropy at high temperatures.
354
355   **5. Measurements of density and compressibility by X-ray diffraction**
356   X-ray diffraction (XRD) is the established and traditional approach for determining the density and
357   compression behaviour of materials. High-P XRD experiments can be performed in either LVPs or DACs, and
358   in recent years are usually carried out at synchrotron sources. Compared with laboratory sources,
359   synchrotrons provide high-energy X-rays that allow for short acquisition times. XRD measurements
360   principally constrain the sample's lattice parameters and crystal structure. Lattice parameters can be used to
361   calculate the (unit cell) volume V of the sample and, if the mass is known, its density. Measurements of unit
362   cell volumes as a function of pressure are now routine, and resulting datasets can be fitted using an
363   appropriate equation of state formalism. The room pressure isothermal bulk modulus $K_{0,T}$ and its pressure
364   derivative at ambient conditions (K_0') can be extracted from the resulting models. These data alone provide
365   an estimate of a material's bulk sound velocity (v_ϕ, Box 1).
366
367   Diffraction experiments are significantly quicker and easier to perform compared with any direct sound wave
368   velocity measurements. The relative ease of the experiments and the long-standing implementation of the
369   technique at global synchrotron sources have generated large datasets for several minerals at high PT, largely
370   by conducting x-ray diffraction in laser-heated DACs. Recent increases in synchrotrons' photon fluxes,
371   combined with developments in detector technology have made XRD experiments even faster than before.

372 Ten years ago, the collection of a single powder diffraction pattern at a state-of-the-art synchrotron facility
373 took a few minutes; the same information can now be derived substantially faster. For example, using novel
374 single photon counting detectors with very high quantum efficiency individual diffraction patterns of
375 (Mg,Fe)O can be collected in a few milliseconds [e.g 10,95,96]. These developments allow for collection of quasi-
376 continuous volume-compression data, from which the elastic isothermal bulk modulus (eq. 4) can be directly
377 determined at any pressure without relying on an equation of state formalism. These developments of time-
378 resolved XRD, in particular when combined with finely controlled compression paths or stress cycles at
379 tailored frequencies facilitated through membrane- or (resistive-heated) piezo-driven DACs[10,96], will no doubt
380 lead to new innovations in the use of synchrotron XRD in high-P experiments. However, XRD measurements
381 do not provide information on the shear modulus of the sample.

383 Both BS and US setups have been coupled with x-ray diffraction at Synchrotron sources[97,98], whilst XRD-BS
384 has additionally been performed in university laboratories[5,99], to measure sound wave velocities and
385 densities simultaneously. This becomes particularly useful for high-PT measurements where the density of
386 the minerals is often poorly known. Moreover, the combination of the Brillouin or ultrasonic results (K_s) and
387 x-ray diffraction allows for calculating an "absolute pressure", i.e. a pressure that is independent of the used
388 pressure standard[5,50,55,97,99,100]. The combination therefore has the potential to eliminate uncertainties in
389 experimental results related to the use of a secondary pressure standard.

391 **6. Outstanding challenges and future directions:**
392 Light scattering methods in the DAC and LVP-ultrasonic interferometry have emerged as the dominant
393 techniques to measure high-PT elastic properties of deep mantle phases. While light scattering in the DAC at
394 pressure of the lower mantle is now routine, the simultaneous generation of high temperature remains highly
395 challenging. Equivalently, LVP experiments can reach temperatures of the mantle adiabat but have not been
396 used to achieve PT conditions beyond the very upper portions of the lower mantle when combined with
397 elasticity measurements. Across both DAC and LVP techniques, experimental data on the seismic properties
398 of most phases now exists at simultaneously high-PT conditions. However, in almost all cases these data are
399 limited to one, or in some cases two, study(ies) that measured polycrystalline seismic properties.
400 Ringwoodite, calcium perovskite, bridgmanite, stishovite and majoritic garnet have been studied using LVP
401 ultrasonics to temperatures of > 1500 K – but data are for a single composition, at limited PT conditions and
402 to date there have been few duplicate measurements. High-PT polycrystalline BS has been used to measure
403 ferropericlase and bridgmanite at 2700 K and ~95 GPa. However, the entirety of these data are limited to 7
404 data points (4 for fp and 3 for bm), each of which is likely to have large uncertainties on the temperatures at
405 experimental conditions. Furthermore, there are no measurements of the seismic properties of NAL-phase,
406 CF-phase, post-stishovite, seifertite or post-perovskite at temperatures above 300 K, and those for wadsleyite
407 are limited to ~ 1000 K. Even for the most-studied lower mantle phase ferropericlase, uncertainties remain
408 regarding the effect of the iron spin transition on the elastic response and the shape of the bulk modulus
409 softening with pressure[8,12,16,53]. And there are still no experimental reported measurements of sound wave
410 velocities across the spin transition region at high T (Fig. 2b). Moreover, our experimental knowledge on the
411 elastic properties of minor phases in the mantle, such as carbonates[101] or hydrous mantle phases[102], as well
412 as melts[103] remains poor or almost non-existent. Examples of some of the high-pressure hydrous mantle
413 phases that have so-far been studied include single-crystal superhydrous phase B, which has been measured
414 by Brillouin spectroscopy at 12 GPa and 700 K[104], whilst Phase D and Phase E have still only been studied at
415 ambient conditions[105-107]. Elastic properties of polycrystalline Ice VII and δ-AlOOH have been studied to much
416 higher pressures extending above 100 GPa[108-110].

418 The bottom line is, experimental datasets are nowhere near suitable. They often remain insufficient for
419 tuning atomistic modelling results or for developing models of seismic properties that can be used to
420 interpret the cause of observed seismic reflections, conversions and or anomalies in tomographic models.
421 We are missing the quantity of data to allow any reliable statistical tests of data quality and/or derived
422 results, and it remains challenging to quantify the real uncertainties on data reported from any single study.
423 Likewise, very few deep mantle minerals with similar chemical composition have been measured by different
424 techniques (e.g. Brillouin and ultrasonics) and comparison of the limited data sets available reveals some

inconsistencies, e.g. see discussions for olivine and wadsleyite in refs. [4,50]. Unfortunately, systematically unravelling the underlying reason is difficult given the small amount of comparable data sets (composition, pressure-/temperature-range). Overall, uncertainties in velocities for any mantle mineral phase at the *PT*-conditions of the Earth's deep mantle cannot be assumed to be known to an accuracy better than ± 1-2%, or in many cases ± 2-5%. The magnitude of typical observed seismic anomalies in tomographic models reach maxima of ± 2-3% at transition zone conditions, but decrease to < 1% in v_p or v_s throughout the lower mantle[e.g.111]. Despite limited tomographic resolution likely masking the true magnitude of anomalies, which will be somewhat larger and more in line with those observed using full waveform inversion techniques[e.g. 112,113], it very quickly becomes clear that reliable interpretations of observed velocity anomalies are challenging.

The current picture is even more incomplete if we consider the range of measurements available that constrain the anisotropy of deep Earth phases. At present such high-*P* datasets are generated solely from DAC-based light-scattering techniques and, aside from olivine, garnet, ringwoodite and ferropericlase, all such data are currently limited to room temperature conditions. Data for bridgmanite, Earth's most abundant mineral, come from only two studies[5,9] that are limited to pressures < 40 GPa (corresponding to a depth of about 1000 km). Moreover, the two studies do not entirely agree in their findings. The chemical complexity of bridgmanite combined with the absence of any other high-pressure single crystal elasticity data on bridgmanite make it virtually impossible to unravel the reason for the apparent discrepancy between the published data. Are the differences related to structural or chemical differences in the studied sample, differences in the employed laboratory setups, and/or the data analysis procedure? Moreover, even if knowledge about the elastic tensor of the major mantle minerals at relevant conditions were to become available, the way that single crystals orient in the mantle – the lattice preferred orientation – needs to be known to model seismic anisotropy observations in the mantle[114,115] and link them to mantle flow patterns.

Additional challenges arise when comparing current experimental results to seismic observations. Elastic properties of lower mantle and transition zone minerals are measured at very high frequencies (MHz-THz), while seismic waves propagate at much lower frequencies (~0.001-100 Hz). It is often assumed that the mantle behaves like a completely elastic material, in which case wave velocities will be independent of frequency (there will be no dispersion). However, dispersion of seismic waves might occur in some parts of the deep mantle. Moreover, seismic attenuation in the mantle[116-118] can occur when processes, such as grain boundary sliding, chemical diffusion, or phase transitions, take place on the same time-scale (or frequency) as the pressure (stress) variations induced by a passing seismic wave. In this case, part of the seismic energy is lost due to coupling to the respective physical/chemical process. In single-phase materials, for example, processes may include the movement of twin walls in tetragonal $CaSiO_3$ or a possible effect of low-spin/high-spin clustering in $(Mg,Fe)O$[119]. In two-phase regions, associated with phase transitions, this may include element diffusion processes required to achieve thermodynamic equilibrium[120-123]. Thus, as well as mapping the first-order effects of elasticity on seismic wave speeds, future experiments should constrain the frequency- and time-dependence of processes in the mantle. Effort needs to be made to further develop methodologies to study seismic dispersion and attenuation at transition zone and lower mantle conditions[122,124].

In summary, it is clear that a significant gap remains between the *PT* conditions that can be routinely accessed in laboratory elasticity experiments and those that exist throughout the majority of our planet's deep interior (Fig. 4). However, as hinted above, progress is gathering pace; the pressure regime in the LVP is ever expanding, with conditions of over 100 GPa achieved using sintered diamond anvils[92], whilst DAC-based resistive heating can now be performed up to ~ 1500 K, and possibly higher, for several hours at a time[125,126]. The latter suffers from practical constraints of how to incorporate bulky vacuum systems or controlled atmosphere setups with light scattering, but is theoretically feasible. However, achievable temperatures are still far short of realistic mantle temperatures. Equally, 100 GPa in the LVP is unlikely to ever become "routine", especially in combination with pulse-echo ultrasonics, but the available pressure regime will continue to expand. Alternatively, as demonstrated up to 1300 K for single crystals of olivine, CO_2 laser heating coupled with BS measurements[4,68] could provide a solution – but these measurements too are far

478 from straightforward. Polycrystalline BS experiments remain the most feasible[6], but the reliability of these
479 measurements remains unclear, as discussed above.
480
481 Whichever route(s) forward, it is clear that theoretical calculations will be an essential component of the
482 attempts to understand the Earth's deep mantle. The challenge is for experiments to provide a sufficient
483 dataset of measured seismic properties to allow careful and thorough validation of atomistic modelling
484 results for each, and every, significant mineral phase. Only once these data exist will theoretical
485 approximations for lower mantle phases be able to be "tuned", and lower the uncertainties on calculated
486 properties to a level where they can be reliably used to interpret seismic properties. In the near future, we
487 can also expect first seismic data of Mars' mantle to emerge from the data collected by the InSight space
488 mission[e.g.127]. Experimental high-PT elasticity data will play a pivotal role in the interpretation of the seismic
489 observations to come, but since the Martian mantle is believed to contain more iron than Earth's mantle,
490 experimental studies need to broaden the compositional range of studied mantle minerals.
491
492 Finally, mineral physics predictions are still most often compared to one-dimensional, radial averaged,
493 profiles of Earth's mantle, e.g. PREM[128] or AK135[129]. These comparisons are convenient and relatively simple
494 to understand, providing a quick evaluation of the properties of any phase relative to a standard velocity
495 profile. However, one-dimensional radial velocity models are averages of the entire range of mantle
496 velocities, and do not represent the velocity of any real mantle portion. Seismic tomography clearly reveals
497 that there are widespread and significant variations of wave speeds throughout the mantle. It is maybe time
498 that we move away from attempts to compare mineral physics predictions to global 1-D average velocity
499 profiles[6]. Interpretations of regional velocity models or global tomography with mineral physics models hold
500 the promise of far more insight into the true nature of our planet's deep interior. No picture about the make-
501 up of our planet's interior is as detailed as the one emerging from seismic techniques – a lot of information
502 is encoded, we just need the data to decipher it.

BOX 1. Seismic Body Waves and Relations to Mineral Physics:

There are two types of seismic body waves travelling through the Earth. **Compressional** (or **primary**) waves travel via particle motion along the wave propagation direction, with velocity v_p. They arrive before **shear** (or **secondary**) waves which travel by a transverse particle motion, with velocity v_s. The propagation velocity of both compressional and shear waves can be related to the isotropic, i.e. direction- and polarization-independent, elastic moduli of the material they are passing through:

$$v_p^2 = \frac{K_s + \frac{4}{3}G}{\rho} \qquad \text{(eq. 1)}$$

$$v_s^2 = \frac{G}{\rho} \qquad \text{(eq.2)}$$

Where ρ=density, K_s=adiabatic bulk modulus, G=shear modulus (also commonly denoted μ).

These two "real" velocities can be combined to define the bulk sound velocity, v_Φ or v_B:

$$v_\phi^2 = \frac{K_s}{\rho} \qquad \text{(eq. 3)}$$

Bulk sound velocity has been widely used because it can be determined from high-P x-ray diffraction experiments as the isothermal bulk modulus (K_T) of any material describes how its volume or density responds to a change of hydrostatic pressure at constant temperature within the elastic regime:

$$K_T = -V(\partial P/\partial V)_T \qquad \text{(eq. 4)}$$

The adiabatic and isothermal bulk moduli are related by the material's thermal expansion (α) and a Grüneisen parameter (γ):

$$K_S = (1 + \alpha_V \gamma T)K_T \qquad \text{(eq. 5)}$$

At room temperature, the difference between the isothermal and adiabatic bulk moduli is often about 1%, so many studies simply use K_T to constrain v_Φ, but this discrepancy significantly increases at mantle temperatures. Another complication of using the bulk sound velocity is that it is seismologically constrained by combining both P- and S-wave models (substitution of eq. 1 and 2 into 3), but these are usually based on different travel paths and/or periods.

$$v_\phi^2 = v_p^2 - \frac{4}{3}v_s^2 \qquad \text{(eq. 6)}$$

It is emphasised that the above relations only hold for perfectly elastic and isotropic materials where no seismic energy is lost through dissipation and seismic wave velocities are not dependent on their direction of travel. In such cases, bulk and shear moduli are substituted by the anisotropic elastic tensor, with the tensor elements referred to as elastic constants (C_{ij}s), Box 2.

BOX 2. Anisotropy and averaging schemes

All minerals, even those with cubic symmetry, are somewhat elastically anisotropic; different directions of the lattice change by different amounts under stress. The full response of any lattice to an external stress (σ) or strain (ε) is described by its elastic tensor (in contracted notation)[1]:

$$\begin{pmatrix} \sigma_1 \\ \sigma_2 \\ \sigma_3 \\ \sigma_4 \\ \sigma_5 \\ \sigma_6 \end{pmatrix} = \begin{pmatrix} c_{11} & c_{12} & c_{13} & c_{14} & c_{15} & c_{16} \\ c_{21} & c_{22} & c_{23} & c_{24} & c_{25} & c_{26} \\ c_{31} & c_{32} & c_{33} & c_{34} & c_{35} & c_{36} \\ c_{41} & c_{42} & c_{43} & c_{44} & c_{45} & c_{46} \\ c_{51} & c_{52} & c_{53} & c_{54} & c_{55} & c_{56} \\ c_{61} & c_{62} & c_{63} & c_{64} & c_{65} & c_{66} \end{pmatrix} \begin{pmatrix} \varepsilon_1 \\ \varepsilon_2 \\ \varepsilon_3 \\ \varepsilon_4 \\ \varepsilon_5 \\ \varepsilon_6 \end{pmatrix} \qquad \text{(eq. 7)}$$

σ_{1-3} and ε_{1-3} are normal and σ_{4-6}, and ε_{4-6} are shear stresses/strains respectively
the c_{ij}'s are the mineral's elastic constants.

Since sound waves are actually stress waves, their apparent velocities will be different in different directions. Whilst the full elastic tensor consists of 36 independent elastic constants, this is reduced for many minerals as multiple elastic constants are constrained by symmetry considerations; e.g. cubic minerals have three unique elastic constants[2]:

$$\begin{pmatrix} \sigma_1 \\ \sigma_2 \\ \sigma_3 \\ \sigma_4 \\ \sigma_5 \\ \sigma_6 \end{pmatrix} = \begin{pmatrix} c_{11} & c_{12} & c_{12} & 0 & 0 & 0 \\ c_{12} & c_{11} & c_{12} & 0 & 0 & 0 \\ c_{12} & c_{12} & c_{11} & 0 & 0 & 0 \\ 0 & 0 & 0 & c_{44} & 0 & 0 \\ 0 & 0 & 0 & 0 & c_{44} & 0 \\ 0 & 0 & 0 & 0 & 0 & c_{44} \end{pmatrix} \begin{pmatrix} \varepsilon_1 \\ \varepsilon_2 \\ \varepsilon_3 \\ \varepsilon_4 \\ \varepsilon_5 \\ \varepsilon_6 \end{pmatrix} \qquad \text{(eq. 8)}$$

Thus, the number of c_{ij}'s requiring definition from single-crystal data is determined by crystal symmetry. Elastic constants are related to the isotropic bulk and shear moduli of a polycrystalline medium of the same mineral by averaging. Such averaging can be performed assuming one of the endmember cases of uniform stress ($\sigma_1 = \sigma_2 = \sigma_3 = -\delta P$; the Reuss bound) or uniform strain ($\varepsilon_1 = \varepsilon_2 = \varepsilon_3 = -\delta P$; the Voigt bound). Whilst for most crystal symmetries the Reuss and Voigt bulk moduli (K_R and K_V respectively) are different, they are equal for cubic symmetry minerals:

$$K_R = K_V = \frac{1}{3}(c_{11} + 2c_{12}) \qquad \text{(eq. 9 – for cubic minerals only)}$$

The same procedure can be undertaken to derive averaged shear moduli, but even for cubic phases this produces two differing values:
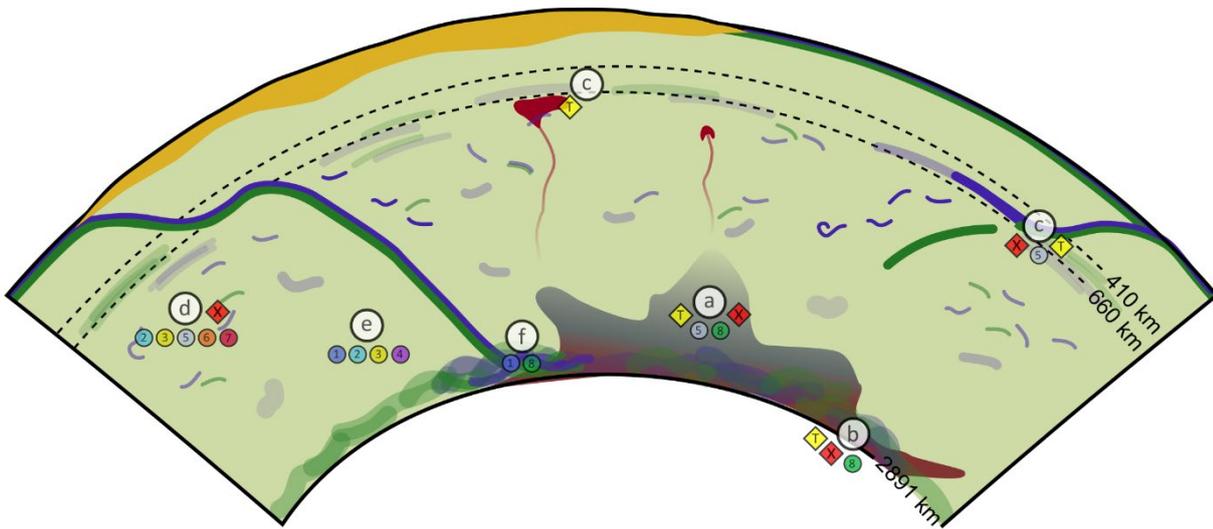
$$G_R = \frac{5(c_{11}-c_{12})c_{44}}{4c_{44}+3(c_{11}-c_{12})} \qquad \text{(eq. 10 – for cubic minerals only)}$$

$$G_V = \frac{1}{5}(3c_{44} + c_{11} - c_{12}) \qquad \text{(eq. 11 – for cubic minerals only)}$$

Whilst the effective moduli must lie between these two bounds, where exactly is unknown. The most common approach when converting c_{ij}'s into bulk moduli are to use the Voigt-Reuss-Hill[3] average, defined in eq. 12 and 13.
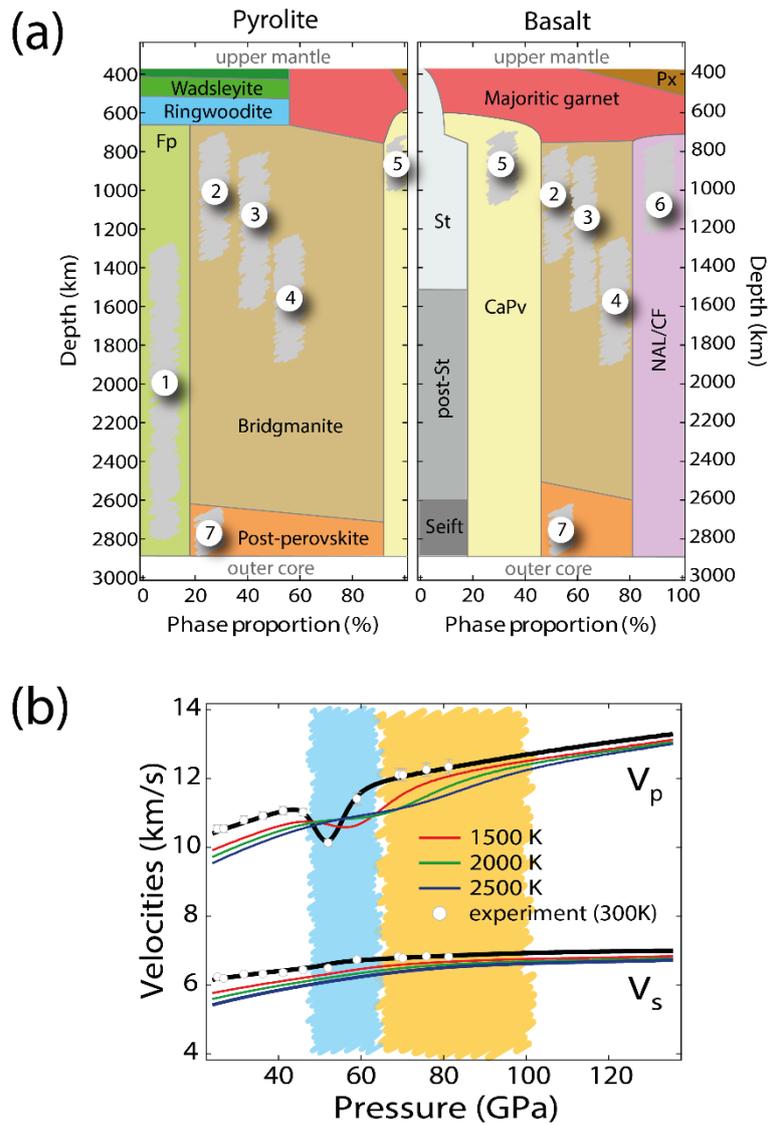
$$K_{VRH} = \frac{1}{2}(K_R + K_V) \text{ or } G_{VRH} = \frac{1}{2}(G_R + G_V) \qquad \text{(eq. 12 and 13)}$$

For phases with low anisotropy, such as majoritic garnet, the Voigt and the Reuss bounds are effectively indistinguishable. However, for highly anisotropic phases, such as ferropericlase at 80 GPa, they vary by ~ 7% for v_s and 3% for v_p (ref. [16]). Another commonly used averaging scheme is the Hashin-Shtrikman approach that results in tighter bounds e.g. [18].
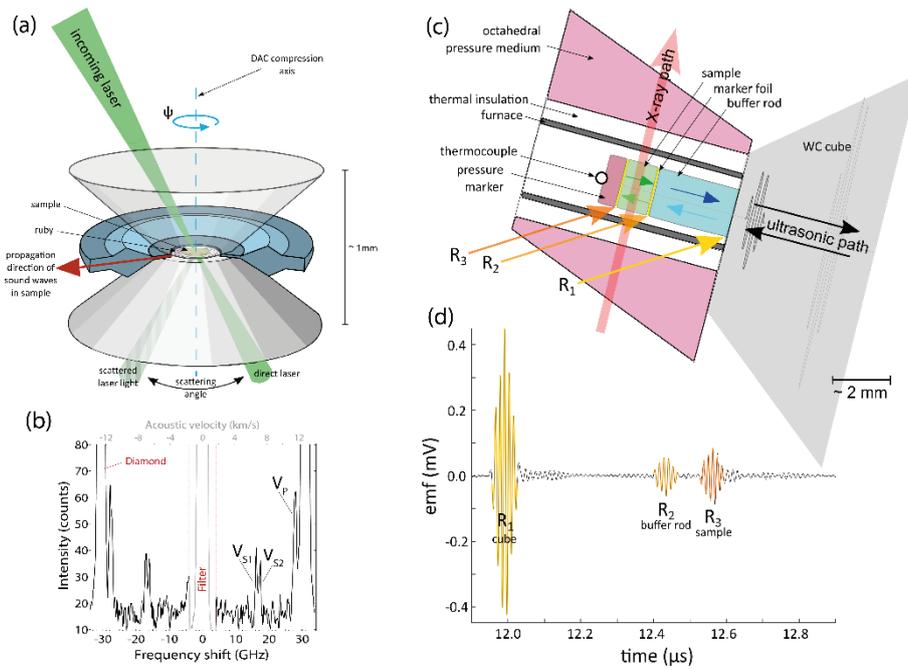
Fig. 1: Interpretive cartoon of Earth's deep mantle based on mineral physics interpretations of seismic observations. Letters in white circles highlight example regions where specific seismic observations have previously been linked to changes in chemistry (X) or temperature (T). Numbers in coloured circles refer to mineralogical features that might provide alternative explanations for the observables, also depicted and labelled in Fig. 2: (a) The seismic signature of Large Low (Shear) Velocity Provinces (LL(S)VPs)[130] has been related to CaPv[11] (5), and post-perovskite[131] (8); (b) Ultra Low Velocity Zones (ULVZs) have been explained by iron-rich (Mg,Fe)O[32,33] or iron-rich post-perovskite[36,103] (8); (c) velocity variations in the transition zone/top of lower mantle have been linked to the low sound wave velocities of cubic CaPv[7] (5); (d) seismic reflectors in the mid-mantle might be related to the spin transition in the NAL-phase[132] (7), the displacive phase transition in stishovite[74,133-135] (6), or the cubic to tetragonal transition in $CaSiO_3$ perovskite[11,136,137] (5); (e) changes in the one-dimensional velocity structure of the lower mantle, as well as lateral seismic heterogeneity have been attributed to the spin transition in ferropericlase[16,138,139] (1), the spin transition in bridgmanite[15,140] (2), a change of the ferric iron content in bridgmanite[5,141,142] (3), or cation re-distribution within bridgmanite[143] (4); (f) seismic anisotropy in the D'' layer has been linked to post-perovskite[144,145] (8), or low-spin ferropericlase[12,17,125] (1).
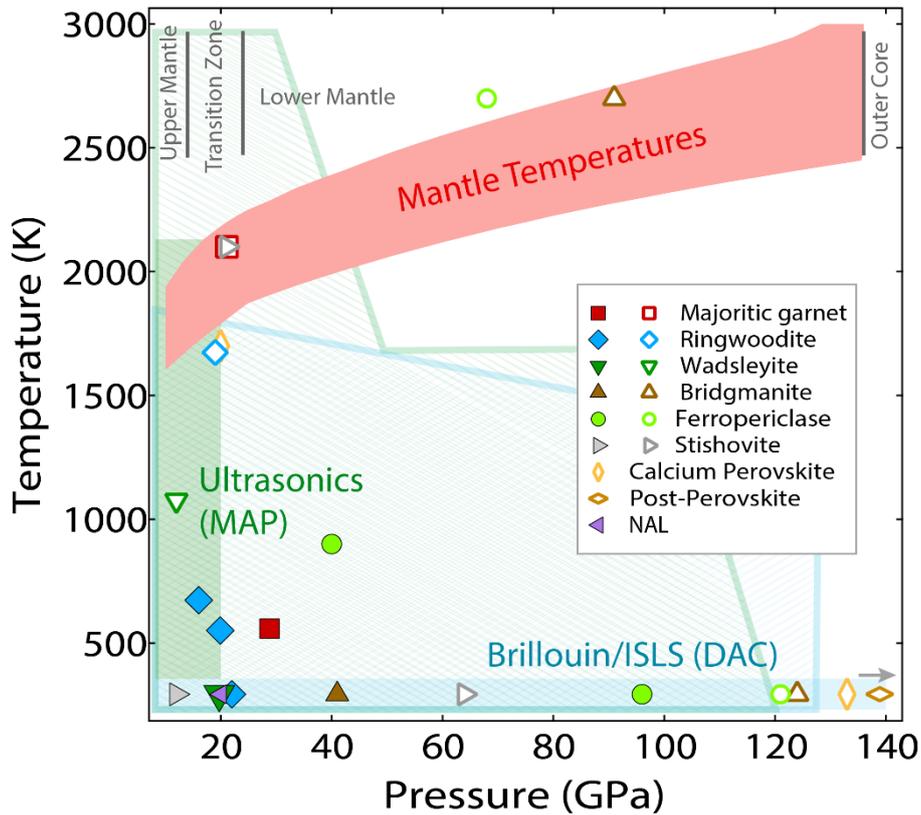
13

Fig. 2: Mineralogy of the transition zone and lower mantle for pyrolitic and mid ocean ridge basalt (MORB) bulk compositions and processes that might affect seismic observables. (a) Mineralogical features that have recently been identified in the lower mantle and have been proposed to explain some of the seismic observables depicted in Fig. 1 are shown: (1) Spin transition of Fe^{2+} in ferropericlase[19,146]; (2) Spin transition of B-site Fe^{3+} in bridgmanite[15,146,147]; (3) decrease of ferric iron content in bridgmanite[5,141]; (4) cation redistribution in bm[140,142,143], (5) tetragonal distortion of calcium silicate perovskite[7,11]; (6) displacive phase change in stishovite; (7) Spin transition in the NAL-phase[132]; (8) post-perovskite transition[148-150]. The approximate depth range over which each process/feature extends is illustrated by the scribbled regions. Fp: Ferropericlase; St: Stishovite; Seift: Seifertite; Px: Pyroxene; NAL: New hexagonal Aluminous Phase; CF: Calcium-ferrite phase. (b) The effect of the iron spin transition in (Mg,Fe)O on seismic velocities. Note the marked drop of V_p at ~50 GPa. Previous measurements of this effect are limited to room temperature (circles). Theoretical work predicts that the spin transition range broadens at lower mantle temperatures (coloured curves), but experimental confirmation is still outstanding. This effect could lead to a less pronounced softening of wave velocities that spreads out over a large pressure range. Note that the complex dependence on pressure and temperature can lead to a situation where an increase of temperature causes V_p to increase (blue scribbled region), an effect that is incompatible with the simple relations currently used to interpret seismic tomography models (slow = hot; fast = cold), as well as a broad region where V_p is more sensitive to temperature than V_s (yellow scribbled region). Figure modified from ref. [16].

Fig. 3: Illustration of high-pressure elasticity experiments. (a) Schematic of a DAC-based Brillouin scattering experiment, showing a magnified view of the sample chamber. The incoming laser beam is focused on a platelet sample in the pressure chamber. A small component of this laser light is scattered by the sample and collected at a defined scattering angle. This scattered light has exchanged energy with sound waves in the sample, which propagate in the direction marked with the red arrow. (b) The frequency content of the scattered light is plotted as intensity vs. frequency shift with respect to the incoming laser light. The spectrum is symmetric since energy can either be gained or lost during the inelastic interaction with sound waves. In the case of an elastically anisotropic single crystal, three contributions can be identified in the spectrum that arise from two shear waves (V_S) and one compressional wave (V_P) propagating in the direction that is probed. The strong contributions at high frequency shifts relate to the diamond-anvils that are trespassed by the laser beam. After a measurement is taken, which can takes several hours at high pressures, the DAC is rotated around the compression direction (blue line in (a)) by a few degrees and another Brillouin spectrum is measured. All velocities measured along different propagation direction, i.e. rotation angles, in the sample are inverted for the elastic constants by employing the Christoffel equation; linking phonon propagation directions, wave velocities, and elastic constants[e.g.2]. Spectrum reproduced from ref. [5]. (c) Schematic of a high-pressure multi-anvil press ultrasonic experiment, with components labelled. MHz frequency sound pulses are passed through one of the WC cubes into the sample via a buffer rod, with reflections returning to the transducer from interfaces R_1 (cube – buffer rod), R_2 (buffer rod – sample) and R_3 (sample – backing medium). X-ray radiography measures the sample length L using marker foils at the top and bottom of the sample. (d) A typical ultrasonic spectrum collected in an experiment, with peaks in intensity resulting from echoes returning from interfaces R_1, R_2 and R_3. The sound wave velocity in the sample can be calculated from $2L/\Delta t$, where Δt is the difference between the arrival time of R_2 and R_3.

Fig. 4: *PT*-conditions covered by published light scattering elasticity measurements in the DAC and ultrasonic experiments in the LVP as compared to the mantle geotherm. The dark shaded regions illustrate the conditions that are routinely achievable for elasticity measurements, whereas the symbols refer to the maximum *PT*-conditions reached in elasticity experiments on specific mantle phases. Solid symbols denote measurements on single crystals, and open symbols refer to polycrystalline measurements. Single-crystal data are plotted for ringwoodite[13,58,64], wadsleyite[50,60], majorite[55], ferropericlase[53,65], bridgmanite[5], NAL-phase[151]. Polycrystalline data are for wadsleyite[152], majoritic garnet[153], ferropericlase (magnesiowüstite)[6,32], bridgmanite[6], stishovite[81,154], CaPv[7,11,82], post-perovskite[77] (measured up to 172 GPa). The scribbled regions shows the approximate range of *PT*-conditions that have been reached using the respective high-*PT* apparatus, but where few or no elasticity measurements have been performed to-date. Green scribbled region: Conditions achievable in the MAP[92]; blue scribbled region: Conditions achievable in the resistive-heated DAC[126]. The laser-heated DAC is capable of reproducing the entire range of *PT*-conditions covered by the figure.

Table 1: Overview of techniques to measure high-*PT* elasticity of mantle minerals. BS: Brillouin Spectroscopy; XRD: X-ray diffraction, IXS: Inelastic x-ray scattering; PSA: picosecond acoustics; ISLS: Impulsive stimulated light scattering; NRIXS: Nuclear resonant inelastic x-ray scattering; US: ultrasonics; SC: single crystal; PC: polycrystal; wad: wadsleyite; rw: ringwoodite; mj: majorite; bm: bridgmanite; fp: ferropericlase; st: stishovite; NAL: ; CF: calcium ferrite phase; ak: akimotoite.

	Method	General Principle	Measured Quantity	Probing Frequency	Derived Property	Limitations	Strength	Time-requirement	Where	Measured TZ/LM minerals (HP or HP/HT)
DAC-based	BS (SC)	Photon-phonon scattering	Frequency shift of laser light	10^9 Hz	V_p, V_s, C_{ij}	transparent sample, V_p not detectable at HP	High-quality data, elastic anisotropy	very high	laboratory	Wad[50,60-63]; Rw[57,58,64,155]; Mj[54-56]; Bm[5,9]; MgO[66,156,157]; Fp[16,17,53,59,65]; (post-)st[158]; NAL/CF[151]
	BS (PC)	Photon-phonon scattering	Frequency shift of laser light	10^9 Hz	V_p, V_s, K_S, G	same as above, sensitivity to grain size, CPO, laser coupling	In-situ synthesis of samples possible	moderate	laboratory	Mj[80]; Bm[6,15,78,79]; Fp[6]; CaPv[82]; (post-)st[81]; Ppv[77]
	XRD	elastic x-ray scattering	lattice parameters, volume	0 Hz	K_T, ρ	no shear modulus	Fast, H*T* routine	low	synchrotron	All materials
	IXS (SC)	Photon-phonon scattering	points on phonon dispersion curve	10^{12} Hz	V_p, V_s, C_{ij}	time-consuming	opaque single-crystals can be measured	high	synchrotron	Fp[12]
	PSA (SC/PC)	Optoacoustic generation/detection of acoustic strains	Time-dependent surface reflectivity	10^9 Hz	V_p, V_s, C_{ij}	Not yet routine	Opaque sample, fast	low	laboratory	No mantle mineral. Metallic samples[42,44]
	ISLS (SC/PC)	Photon-phonon inelastic scattering	Diffracted intensity in time domain	10^9 Hz	V_p, V_s, C_{ij}	Limited information for V_s	V_p at H*P*	moderate	laboratory	Bm[9,15]; Fp[8,53],
	NRIXS (SC/PC)	Photon scattering from nuclear excitation of ^{57}Fe	Partial Phonon Density of States (PDOS)	range	V_{Debye}, V_p, V_s,	Derivation of V_p and V_S requires equation of state, ^{57}Fe needed	Opaque samples can be measured	moderate	synchrotron	Fp/Mw[32-35]; Ppv[36]
	GHz interferometry (SC)	Generation of sound wave by piezo-actuator	Travel time	10^9 Hz	V_p, V_s, C_{ij}	Limited to <10 GPa	Opaque samples can be measured	moderate (?)	Laboratory	Rw[159]; Fp[39]
LVP-based	US (PC)	Generation of sound wave by piezo-actuator	Travel time, Sample length	10^6 Hz	V_p, V_s, K_S, G	data sensitive to grain size, preferred orientation, limited P-range	High-temperatures can be routinely achieved	medium	synchrotron	Wad[152,160,161]; Rw[14,162]; Mj[163-165]; Bm[85,166,167]; Fp[168]; CaPv[7,11]; St[154], Ak[169]
	XRD	elastic x-ray scattering	lattice parameters, volume	0 Hz	K_T, ρ	no shear modulus	Fast, H*T* routine	low	synchrotron	Most materials

References:

1. Nye, J. *Physical Properties of Crystals*. (Clarendon Press, 1985).
2. Speziale, S., Marquardt, H. & Duffy, T. S. Brillouin Scattering in Geosciences. in *Spectroscopic methods in mineralogy and materials science* **78**, 543-603 (2014).
3. Hill, R. The elastic behaviour of a crystalline aggregate. *Proc Phys Soc Lond A* **65**, 349-354 (1952).
4. Zhang, J. S. & Bass, J. D. Sound velocities of olivine at high pressures and temperatures and the composition of Earth's upper mantle. *Geophysical Research Letters* **43**, 9611-9618 (2016).
5. Kurnosov, A., Marquardt, H., Frost, D. J., Ballaran, T. B. & Ziberna, L. Evidence for a Fe^{3+}-rich pyrolitic lower mantle from (Al,Fe)-bearing bridgmanite elasticity data. *Nature* **543**, 543-546 (2017).
6. Murakami, M., Ohishi, Y., Hirao, N. & Hirose, K. A perovskitic lower mantle inferred from high-pressure, high-temperature sound velocity data. *Nature* **485**, 90-94 (2012).
7. Gréaux, S. *et al.* Sound velocity of $CaSiO_3$ perovskite suggests the presence of basaltic crust in the Earth's lower mantle. *Nature* **565**, 218-221 (2019).
8. Crowhurst, J. C., Brown, J. M., Goncharov, A. F. & Jacobsen, S. D. Elasticity of (Mg,Fe)O through the spin transition of iron in the lower mantle. *Science* **319**, 451-453 (2008).
9. Fu, S. *et al.* Single-crystal elasticity of (Al,Fe)-bearing bridgmanite and seismic shear wave radial anisotropy at the topmost lower mantle. *Earth and Planetary Science Letters* **518**, 116-126 (2019).
10. Marquardt, H. *et al.* Elastic Softening of $(Mg_{0.8}Fe_{0.2})O$ Ferropericlase Across the Iron Spin Crossover Measured at Seismic Frequencies. *Geophysical Research Letters* **45**, 6862-6868 (2018).
11. Thomson, A. *et al.* Calcium silicate perovskite's acoustic velocities can explain LLSVPs in Earth's lower mantle. *Nature* **572**, 643-647 (2019).
12. Antonangeli, D. *et al.* Spin Crossover in Ferropericlase at High Pressure: A Seismologically Transparent Transition? *Science* **331**, 64-67 (2011).
13. Schulze, K. *et al.* Seismically Invisible Water in Earth's Transition Zone? *Earth and Planetary Science Letters* **498**, 9-16 (2018).
14. Higo, Y., Inoue, T., Irifune, T., Funakoshi, K.-i. & Li, B. Elastic wave velocities of $(Mg_{0.91}Fe_{0.09})_2SiO_4$ ringwoodite under P-T conditions of the mantle transition region. *Phys. Earth Planet. Inter.* **166**, 167-174 (2008).
15. Fu, S. *et al.* Abnormal Elasticity of Fe-Bearing Bridgmanite in the Earth's Lower Mantle. *Geophysical Research Letters* **45**, 4725-4732 (2018).
16. Marquardt, H., Speziale, S., Reichmann, H. J., Frost, D. J. & Schilling, F. R. Single-crystal elasticity of $(Mg_{0.9}Fe_{0.1})O$ to 81 GPa. *Earth and Planetary Science Letters* **287**, 345-352 (2009).
17. Marquardt, H. *et al.* Elastic Shear Anisotropy of Ferropericlase in Earth's Lower Mantle. *Science* **324**, 224-226 (2009).
18. Watt, J. P., Davies, G. F. & O'Connell, R. J. The elastic properties of composite materials. *Rev. Geophys.* **14**, 541-563 (1976).
19. Badro, J. *et al.* Iron partitioning in Earth's mantle: toward a deep lower mantle discontinuity. *Science* **300**, 789-791 (2003).
20. Wu, Z. & Wentzcovitch, R. M. Spin crossover in ferropericlase and velocity heterogeneities in the lower mantle. *Proc. Natl. Acad. Sci.* **111**, 10468–10472 (2014).
21. Wu, Z. Velocity structure and composition of the lower mantle with spin crossover in ferropericlase. *Journal of Geophysical Research: Solid Earth* **121**, 2304-2314 (2016).
22. Stixrude, L. & Lithgow-Bertelloni, C. Thermodynamics of mantle minerals - I. Physical properties. *Geophys. J. Int.* **162**, 610-632 (2005).
23. Karki, B. B., Stixrude, L. & Wentzcovitch, R. M. High-pressure elastic properties of major materials of Earth's mantle from first principles. *Rev. Geophys.* **39**, 507-534 (2001).
24. Bass, J. D. Techniques for measuring High *P/T* Elasticity. in *Treatise on Geophysics - Mineral Physics* (2007).
25. Angel, R. J., Jackson, J. M., Reichmann, H. J. & Speziale, S. Elasticity measurements on minerals: a review. *European Journal of Mineralogy* **21**, 525-550 (2009).
26. Isaak, D. G., Anderson, O. L. & Goto, T. Measured elastic moduli of single-crystal MgO up to 1800 K. *Physics and Chemistry of Minerals* **16**, 704-713 (1989).

653 27 Isaak, D. G. *et al.* The temperature dependence of the elasticity of Fe-bearing wadsleyite. *Phys.*
654   *Earth Planet. Inter.* **182**, 107-112 (2010).
655 28 Loong, C.-K. Inelastic Scattering and Applications. in *Reviews in Mineralogy & Geochemistry:*
656   *Neutron Scattering in Earth Sciences* **63**, 233-254 (2006).
657 29 Fiquet, G. *et al.* Application of inelastic X-ray scattering to the measurements of acoustic wave
658   velocities in geophysical materials at very high pressure. *Phys. Earth Planet. Inter.* **143-144**, 5-18
659   (2004).
660 30 Burkel, E. Phonon spectroscopy by inelastic x-ray scattering. *Rep. Prog. Phys*, 171 (2000).
661 31 Sturhahn, W. Nuclear resonant spectroscopy. *Journal of Physics: Condensed Matter* **16**, S497-S530
662   (2004).
663 32 Wicks, J. K., Jackson, J. M. & Sturhahn, W. Very low sound velocities in iron-rich (Mg,Fe)O:
664   Implications for the core-mantle boundary region. *Geophysical Research Letters* **37**, L15304 (2010).
665 33 Wicks, J. K., Jackson, J. M., Sturhahn, W. & Zhang, D. Sound velocity and density of
666   magnesiowüstites: Implications for ultralow-velocity zone topography. *Geophysical Research*
667   *Letters* **44**, 2148-2158 (2017).
668 34 Finkelstein, G. J. *et al.* Strongly Anisotropic Magnesiowüstite in Earth's Lower Mantle. *J. Geophys.*
669   *Res.* **123**, 4740-4750 (2018).
670 35 Lin, J.-F. *et al.* Sound velocities of ferropericlase in the Earth`s lower mantle. *Geophysical Research*
671   *Letters* **33**, L22304 (2006).
672 36 Mao, W. L. *et al.* Iron-Rich Post-Perovskite and the Origin of Ultralow-Velocity Zones. *Science* **312**,
673   564-565 (2006).
674 37 McCammon, C. *et al.* Sound velocities of bridgmanite from density of states determined by nuclear
675   inelastic scattering and first-principles calculations. *Progress in Earth and Planetary Science* **3**, 10
676   (2016).
677 38 Jacobsen, S. D. *et al.* Structure and elasticity of single-crystal (Mg,Fe)O and a new method of
678   generating shear waves for gigahertz ultrasonic interferometry. *J. Geophys. Res.* **107**, 2037 (2002).
679 39 Jacobsen, S. D., Spetzler, H., Reichmann, H. J. & Smyth, J. R. Shear waves in the diamond-anvil cell
680   reveal pressure-induced instability in (Mg,Fe)O. *Proc. Natl. Acad. Sci.* **101**, 5867-5871 (2004).
681 40 Jacobsen, S. D. *et al.* Gigahertz ultrasonic interferometry at high P and T: new tools for obtaining a
682   thermodynamic equation of state. *Journal of Physics: Condensed Matter* **14**, 11525-11530 (2002).
683 41 Li, B. & Liebermann, R. C. Study of the Earth's interior using measurements of sound velocities in
684   minerals by ultrasonic interferometry. *Phys. Earth Planet. Inter.* **233**, 135--153 (2014).
685 42 Decremps, F. *et al.* Sound velocity of iron up to 152 GPa by picosecond acoustics in diamond anvil
686   cell. *Geophysical Research Letters* **41**, 1459-1464 (2014).
687 43 Kuriakose, M. *et al.* Picosecond laser ultrasonics for imaging of transparent polycrystalline materials
688   compressed to megabar pressures. *Ultrasonics* **69**, 259-267 (2016).
689 44 Edmund, E. *et al.* Picosecond Acoustics Technique to Measure the Sound Velocities of Fe-Si Alloys
690   and Si Single-Crystals at High Pressure. *Minerals* **10**, 214 (2020).
691 45 Whitfield, C. H., Brody, E. M. & Bassett, W. A. Elastic moduli of NaCl by Brillouin scattering at high
692   pressure in a diamond anvil cell. *Review of Scientific Instruments* **47**, 942-947 (1976).
693 46 Sinogeikin, S. V. & Bass, J. D. Single-crystal elasticity of pyrope and MgO to 20 GPa by Brillouin
694   scattering in the diamond cell. *Phys. Earth Planet. Inter.* **120**, 43-62 (2000).
695 47 Speziale, S. & Duffy, T. S. Single-crystal elastic constants of fluorite (CaF_2) to 9.3 GPa. *Physics and*
696   *Chemistry of Minerals* **29**, 465-472 (2002).
697 48 Kurnosov, A., Marquardt, H., Frost, D. J., Ballaran, T. B. & Ziberna, L. Kurnosov et al. reply. *Nature*
698   **564**, E27-E31 (2018).
699 49 Lin, J.-F., Mao, Z., Yang, J. & Fu, S. Elasticity of lower-mantle bridgmanite. *Nature* **564**, E18-E26
700   (2018).
701 50 Buchen, J. *et al.* High-pressure single-crystal elasticity of wadsleyite and the seismic signature of
702   water in the shallow transition zone. *Earth and Planetary Science Letters* **498**, 77-87 (2018).
703 51 Mao, Z. *et al.* Elasticity of single-crystal olivine at high pressures and temperatures. *Earth and*
704   *Planetary Science Letters* **426**, 204-215 (2015).

705 52 Schulze, K., Buchen, J., Marquardt, K. & Marquardt, H. Multi-sample loading technique for
706 comparative physical property measurements in the diamond-anvil cell. *High Press. Res.* **37**, 159-
707 169 (2017).
708 53 Yang, J., Tong, X., Lin, J.-F., Okuchi, T. & Tomioka, N. Elasticity of Ferropericlase across the Spin
709 Crossover in the Earth's Lower Mantle. *Sci Rep* **5**, 17188 (2015).
710 54 Murakami, M., Sinogeikin, S. V., Litasov, K., Ohtani, E. & Bass, J. D. Single-crystal elasticity of iron-
711 bearing majorite to 26 GPa: Implications for seismic velocity structure of the mantle transition
712 zone. *Earth and Planetary Science Letters* **274**, 339-345 (2008).
713 55 Pamato, M. G. *et al.* Single crystal elasticity of majoritic garnets: Stagnant slabs and thermal
714 anomalies at the base of the transition zone. *Earth and Planetary Science Letters* **451**, 114-124
715 (2016).
716 56 Sanchez-Valle, C., Wang, J. & Rohrbach, A. Effect of calcium on the elasticity of majoritic garnets
717 and the seismic gradients in the mantle transition zone. *Phys. Earth Planet. Inter.* **293**, 106272
718 (2019).
719 57 Sinogeikin, S. V., Bass, J. D. & Katsura, T. Single-crystal elasticity of gamma-$(Mg_{0.91}Fe_{0.09})_2SiO_4$ to high
720 pressures and to high temperatures. *Geophysical Research Letters* **28**, 4335-4338 (2001).
721 58 Wang, J., Sinogeikin, S., Inoue, T. & Bass, J. D. Elastic properties of hydrous ringwoodite at high-
722 pressure conditions. *Geophysical Research Letters* **33**, L14308 (2006).
723 59 Jackson, J. M. *et al.* Single-crystal elasticity and sound velocities of $(Mg_{0.94}Fe_{0.06})O$ ferropericlase to
724 20 GPa. *J. Geophys. Res.* **111**, B09203 (2006).
725 60 Wang, J., Bass, J. D. & Kastura, T. Elastic properties of iron-bearing wadsleyite to 17.7 GPa:
726 Implications for mantle mineral models. *Phys. Earth Planet. Inter.* **228**, 92-96 (2014).
727 61 Mao, Z. *et al.* Effect of hydration on the single-crystal elasticity of Fe-bearing wadsleyite to 12 GPa.
728 *American Mineralogist* **96**, 1606-1612 (2011).
729 62 Mao, Z. *et al.* Elasticity of hydrous wadsleyite to 12 GPa: Implications for Earth's transition zone.
730 *Geophysical Research Letters* **35**, L21305 (2008).
731 63 Zha, C.-s. *et al.* Single-crystal elasticity of beta-Mg_2SiO_4 to the pressure of the 410 km seismic
732 discontinuity in the Earth's mantle. *Earth and Planetary Science Letters* **147**, E9-E15 (1997).
733 64 Mao, Z. *et al.* Sound velocities of hydrous ringwoodite to 16 GPa and 673 K. *Earth and Planetary*
734 *Science Letters* **331–332**, 112-119 (2012).
735 65 Yang, J. *et al.* Elasticity of ferropericlase and seismic heterogeneity in the Earth's lower mantle.
736 *Journal of Geophysical Research: Solid Earth* **121** (2016).
737 66 Fan, D. *et al.* Elasticity of single-crystal periclase at high pressure and temperature: The effect of
738 iron on the elasticity and seismic parameters of ferropericlase in the lower mantle. *American*
739 *Mineralogist* **104**, 262-275 (2019).
740 67 Kriesel, J. M. *et al.* in *SPIE Defense, Security, and Sensing.* 10 (SPIE).
741 68 Kurnosov, A., Marquardt, H., Dubrovinsky, L. & Potapkin, V. A waveguide-based flexible CO_2-laser
742 heating system for diamond-anvil cell applications. *Compt Rend Geosc* **351**, 280-285 (2019).
743 69 Zhang, J. S., Bass, J. D. & Zhu, G. Single-crystal Brillouin spectroscopy with CO_2 laser heating and
744 variable q. *Review of Scientific Instruments* **86**, 063905 (2015).
745 70 Sinogeikin, S. V., Lakshtanov, D. L., Nicholas, J. D. & Bass, J. D. Sound velocity measurements on
746 laser-heated MgO and Al_2O_3. *Phys. Earth Planet. Inter.* **143**, 575-586 (2004).
747 71 Sinogeikin, S. V., Lakshtanov, D. L., Nicholas, J. D., Jackson, J. M. & Bass, J. D. High temperature
748 elasticity measurements on oxides by Brillouin spectroscopy with resistive and IR laser heating.
749 *Journal of the European Ceramic Society* **25**, 1313-1324 (2005).
750 72 Marquardt, H. *et al.* Elastic Properties of MgO Nano-crystals and Grain Boundaries to High
751 Pressures. *Phys. Rev. B* **84**, 064131 (2011).
752 73 Speziale, S., Marquardt, H. & Liermann, H.-P. Approaches to constrain single-crystal elastic
753 properties from Brillouin scattering of polycrystalline samples. *High Press. Res.* **33**, 607-621 (2013).
754 74 Buchen, J. *et al.* Equation of State of Polycrystalline Stishovite Across the Tetragonal-Orthorhombic
755 Phase Transition. *J. Geophys. Res.* **123**, 7347-7360 (2018).
756 75 Marquardt, H., Speziale, S., Jahn, S., Ganschow, S. & Schilling, F. R. Single-crystal elastic properties
757 of $(Y,Yb)_3Al_5O_{12}$. *Journal of Applied Physics* **106**, 093519-093515 (2009).

758   76   Sinogeikin, S. V., Zhang, J. & Bass, J. D. Elasticity of single crystal and polycrystalline MgSiO$_3$
759   perovskite by Brillouin spectroscopy. *Geophysical Research Letters* **31**, L06620 (2004).
760   77   Murakami, M. *et al.* Sound velocity of MgSiO$_3$ post-perovskite phase; a constraint on the D"
761   discontinuity. *Earth and Planetary Science Letters* **259**, 18-23 (2007).
762   78   Jackson, J. M., Zhang, J., Shu, J., Sinogeikin, S. V. & Bass, J. D. High-pressure sound velocities and
763   elasticity of aluminous MgSiO$_3$ perovskite to 45 GPa: Implications for lateral heterogeneity in
764   Earth's lower mantle. *Geophysical Research Letters* **32**, L21305 (2005).
765   79   Murakami, M., Sinogeikin, S. V., Hellwig, H., Bass, J. D. & Li, J. Sound velocity of MgSiO$_3$ perovskite
766   to Mbar pressure. *Earth and Planetary Science Letters* **256**, 47-54 (2007).
767   80   Sinogeikin, S. V. & Bass, J. D. Elasticity of majorite and a majorite-pyrope solid solution to high
768   pressure; implications for the transition zone. *Geophysical Research Letters* **29**, 1017 (2002).
769   81   Asahara, Y. *et al.* Acoustic velocity measurements for stishovite across the post-stishovite phase
770   transition under deviatoric stress: Implications for the seismic features of subducting slabs in the
771   mid-mantle. *American Mineralogist* **98**, 2053-2062 (2013).
772   82   Kudo, Y. *et al.* Sound velocity measurements of CaSiO$_3$ perovskite to 133GPa and implications for
773   lowermost mantle seismic anomalies. *Earth and Planetary Science Letters* **349-350**, 1-7 (2012).
774   83   Abramson, E. H., Brown, J. M. & Slutsky, L. J. Applications of impulsive stimulated scattering in the
775   earth and planetary sciences. *Annual Review of Physical Chemistry* **50**, 279-313 (1999).
776   84   Li, B. & Liebermann, R. C. High-Pressure Geoscience Special Feature: Indoor seismology by probing
777   the Earth's interior by using sound velocity measurements at high pressures and temperatures.
778   *Proc. Natl. Acad. Sci.* **104**, 9145-9150 (2007).
779   85   Chantel, J., Frost, D. J., McCammon, C. A., Jing, Z. & Wang, Y. Acoustic velocities of pure and iron-
780   bearing magnesium silicate perovskite measured to 25 GPa and 1200 K. *Geophysical Research*
781   *Letters* **39**, L19307 (2012).
782   86   Li, B., Kung, J. & Liebermann, R. C. Modern techniques in measuring elasticity of Earth materials at
783   high pressure and high temperature using ultrasonic interferometry in conjunction with
784   synchrotron X-radiation in multi-anvil apparatus. *Phys. Earth Planet. Inter.* **143**, 559--574 (2004).
785   87   Whitaker, M. L., Baldwin, K. J. & Huebsch, W. R. DIASCoPE: Directly integrated acoustic system
786   combined with pressure experiments - A new method for fast acoustic velocity measurements at
787   high pressure. *Review of Scientific Instruments* **88**, 034901 (2017).
788   88   Chen, G., Liebermann, R. C. & Weidner, D. J. Elasticity of Single-Crystal MgO to 8 Gigapascals and
789   1600 Kelvin. *Science* **280**, 1913-1916 (1998).
790   89   Jacobsen, S. D., Smyth, J. R., Spetzler, H., Holl, C. M. & Frost, D. J. Sound velocities and elastic
791   constants of iron-bearing hydrous ringwoodite. *Phys. Earth Planet. Inter.* **143**, 47-56 (2004).
792   90   Cook, R. K. Variation of Elastic Constants and Static Strains with Hydrostatic Pressure: A Method for
793   Calculation from Ultrasonic Measurements. *Journal of the Acoustical Society of America* **29**, 445--
794   449 (1957).
795   91   Kunimoto, T., Irifune, T., Tange, Y. & Wada, K. Pressure generation to 50 GPa in Kawai-type
796   multianvil apparatus using newly developed tungsten carbide anvils. *High Press. Res.* **36**, 97--104
797   (2016).
798   92   Yamazaki, D. *et al.* High-pressure generation in the Kawai-type multianvil apparatus equipped with
799   tungsten-carbide anvils and sintered-diamond anvils, and X-ray observation on CaSnO$_3$ and
800   (Mg,Fe)SiO$_3$. *Compt Rend Geosc* **351**, 253-259 (2019).
801   93   Higo, Y., Irifune, T. & Funakoshi, K. I. Simultaneous high-pressure high-temperature elastic velocity
802   measurement system up to 27 GPa and 1873 K using ultrasonic and synchrotron X-ray techniques.
803   *Review of Scientific Instruments* **89**, 014501 (2018).
804   94   Jing, Z., Yu, T., Xu, M., Chantel, J. & Wang, Y. High-Pressure Sound Velocity Measurements of
805   Liquids Using In Situ Ultrasonic Techniques in a Multianvil Apparatus. *Minerals* **10**, 126 (2020).
806   95   Pennicard, D. *et al.* LAMBDA 2M GaAs—A multi-megapixel hard X-ray detector for synchrotrons. *J*
807   *Instr* **13**, C01026 (2018).
808   96   Jenei, Z. *et al.* New dynamic diamond anvil cells for tera-pascal per second fast compression x-ray
809   diffraction experiments. *Review of Scientific Instruments* **90**, 065114 (2019).

810   97   Sinogeikin, S. *et al.* Brillouin spectrometer interfaced with synchrotron radiation for simultaneous x-
811   ray density and acoustic velocity measurements. *Review of Scientific Instruments* **77**, 103905-
812   103911 (2006).

813   98   Murakami, M., Asahara, Y., Ohishi, Y., Hirao, N. & Hirose, K. Development of in situ Brillouin
814   spectroscopy at high pressure and high temperature with synchrotron radiation and infrared laser
815   heating system: Application to the Earth's deep interior. *Phys. Earth Planet. Inter.* **174**, 282-291
816   (2009).

817   99   Trots, D. M. *et al.* The Sm:YAG primary fluorescence pressure scale. *Journal of Geophysical*
818   *Research: Solid Earth* **118**, 2013JB010519 (2013).

819   100   Matsui, M., Higo, Y., Okamoto, Y., Irifune, T. & Funakoshi, K.-I. Simultaneous sound velocity and
820   density measurements of NaCl at high temperatures and pressures: Application as a primary
821   pressure standard. *American Mineralogist* **97**, 1670-1675 (2012).

822   101   Isshiki, M. *et al.* Stability of magnesite and its high-pressure form in the lowermost mantle. *Nature*
823   **427**, 60-63 (2004).

824   102   Nishi, M. *et al.* Stability of hydrous silicate at high pressures and water transport to the deep lower
825   mantle. *Nat. Geosci.* **7**, 224-227 (2014).

826   103   Fu, S. *et al.* Melting behavior of the lower-mantle ferropericlase across the spin crossover:
827   Implication for the ultra-low velocity zones at the lowermost mantle. *Earth and Planetary Science*
828   *Letters* **503**, 1-9 (2018).

829   104   Li, X. *et al.* Elasticity of single-crystal superhydrous phase B at simultaneous high pressure-
830   temperature conditions. *Geophysical Research Letters* **43**, 8458-8465 (2016).

831   105   Liu, L.-g., Okamoto, K., Yang, Y.-j., Chen, C.-c. & Lin, C.-C. Elasticity of single-crystal phase D (a dense
832   hydrous magnesium silicate) by Brillouin spectroscopy. *Solid State Communications* **132**, 517-520
833   (2004).

834   106   Rosa, A. D., Sanchez-Valle, C. & Ghosh, S. Elasticity of phase D and implication for the degree of
835   hydration of deep subducted slabs. *Geophysical Research Letters* **39** (2012).

836   107   Satta, N. *et al.* Single-crystal elasticity of iron-bearing phase E and seismic detection of water in
837   Earth's upper mantle. *American Mineralogist* **104**, 1526 (2019).

838   108   Ahart, M. *et al.* Brillouin scattering of H_2O ice to megabar pressures. *J. Chem. Phys.* **134**, 124517
839   (2011).

840   109   Zhang, J., Hao, M., Ren, Z. & Chen, B. The extreme acoustic anisotropy and fast sound velocities of
841   cubic high-pressure ice polymorphs at Mbar pressure. *Applied Physics Letters* **114**, 191903 (2019).

842   110   Mashino, I., Murakami, M. & Ohtani, E. Sound velocities of δ-AlOOH up to core-mantle boundary
843   pressures with implications for the seismic anomalies in the deep mantle. *Journal of Geophysical*
844   *Research: Solid Earth* **121**, 595-609 (2016).

845   111   Koelemeijer, P., Ritsema, J., Deuss, A. & van Heijst, H.-J. SP12RTS: a degree-12 model of shear- and
846   compressional-wave velocity for Earth's mantle. *Geophys. J. Int.* **204**, 1024-1039 (2016).

847   112   Borgeaud, A. F. E., Kawai, K. & Geller, R. J. Three-Dimensional S Velocity Structure of the Mantle
848   Transition Zone Beneath Central America and the Gulf of Mexico Inferred Using Waveform
849   Inversion. *Journal of Geophysical Research: Solid Earth* **124**, 9664-9681 (2019).

850   113   Deschamps, F., Konishi, K., Fuji, N. & Cobden, L. Radial thermo-chemical structure beneath Western
851   and Northern Pacific from seismic waveform inversion. *Earth and Planetary Science Letters* **520**,
852   153-163 (2019).

853   114   Wenk, H.-R., Cottaar, S., Tomé, C. N., McNamara, A. & Romanowicz, B. Deformation in the
854   lowermost mantle: From polycrystal plasticity to seismic anisotropy. *Earth and Planetary Science*
855   *Letters* **306**, 33-45 (2011).

856   115   Romanowicz, B. & Wenk, H.-R. Anisotropy in the deep Earth. *Phys. Earth Planet. Inter.* **269**, 58-90
857   (2017).

858   116   Zhang, B., Ni, S. & Chen, Y. Seismic attenuation in the lower mantle beneath Northeast China
859   constrained from short-period reflected core phases at short epicentral distances. *Earth and*
860   *Planetary Physics* **3**, 537-546 (2019).

861   117   Liu, C. & Grand, S. P. Seismic attenuation in the African LLSVP estimated from PcS phases. *Earth and*
862   *Planetary Science Letters* **489**, 8-16 (2018).

863 118 Hwang, Y. K. & Ritsema, J. Radial Q_μ structure of the lower mantle from teleseismic body-wave
864 spectra. *Earth and Planetary Science Letters* **303**, 369-375 (2011).

865 119 Carpenter, M. A. & Zhang, Z. Anelasticity maps for acoustic dissipation associated with phase
866 transitions in minerals. *Geophys. J. Int.* **186**, 279-295 (2011).

867 120 Perrillat, J. P. *et al.* Kinetics of the olivine–ringwoodite transformation and seismic attenuation in
868 the Earth's mantle transition zone. *Earth and Planetary Science Letters* **433**, 360-369 (2016).

869 121 Li, L. Bulk attenuation in the earth's mantle due to phase transitions. *Phys. Earth Planet. Inter.* **183**,
870 473-477 (2010).

871 122 Li, L. & Weidner, D. J. Effect of phase transitions on compressional-wave velocities in the Earth's
872 mantle. *Nature* **454**, 984-986 (2008).

873 123 Ricard, Y., Matas, J. & Chambat, F. Seismic attenuation in a phase change coexistence loop. *Phys.*
874 *Earth Planet. Inter.* **176**, 124-131 (2009).

875 124 Faul, U. & Jackson, I. Transient Creep and Strain Energy Dissipation: An Experimental Perspective.
876 *Annual Review of Earth and Planetary Sciences* **43**, 541-569 (2015).

877 125 Immoor, J. *et al.* Evidence for {100}<011> slip in ferropericlase in Earth's lower mantle from high-
878 pressure/high-temperature experiments. *Earth and Planetary Science Letters* **489**, 251-257 (2018).

879 126 Immoor, J. *et al.* An improved setup for radial diffraction experiments at high pressures and high
880 temperatures in a resistive graphite-heated diamond anvil cell. *Review of Scientific Instruments* **91**,
881 045121 (2020).

882 127 Banerdt, W. B. *et al.* Initial results from the InSight mission on Mars. *Nat. Geosci.* **13**, 183-189
883 (2020).

884 128 Dziewonski, A. M. & Anderson, D. L. Preliminary reference Earth model. *Phys. Earth Planet. Inter.*
885 **25**, 297-356 (1981).

886 129 Kennett, B. L. N., Engdahl, E. R. & Buland, R. Constraints on seismic velocities in the Earth from
887 traveltimes. *Geophys. J. Int.* **122**, 108-124 (1995).

888 130 Garnero, E. J., McNamara, A. K. & Shim, S.-H. Continent-sized anomalous zones with low seismic
889 velocity at the base of Earth's mantle. *Nat. Geosci.* **9**, 481-489 (2016).

890 131 Koelemeijer, P., Schuberth, B. S. A., Davies, D. R., Deuss, A. & Ritsema, J. Constraints on the
891 presence of post-perovskite in Earth's lowermost mantle from tomographic-geodynamic model
892 comparisons. *Earth and Planetary Science Letters* **494**, 226-238 (2018).

893 132 Wu, Y. *et al.* Spin transition of ferric iron in the NAL phase: Implications for the seismic
894 heterogeneities of subducted slabs in the lower mantle. *Earth and Planetary Science Letters* **434**,
895 91-100 (2016).

896 133 Vinnik, L. P., Oreshin, S. I., Speziale, S. & Weber, M. Mid-mantle layering from SKS receiver
897 functions. *Geophysical Research Letters* **37**, L24302 (2010).

898 134 Jenkins, J., Deuss, A. & Cottaar, S. Converted phases from sharp 1000 km depth mid-mantle
899 heterogeneity beneath Western Europe. *Earth and Planetary Science Letters* **459**, 196-207 (2017).

900 135 Lakshtanov, D. L. *et al.* The post-stishovite phase transition in hydrous alumina-bearing SiO_2 in the
901 lower mantle of the earth. *Proc. Natl. Acad. Sci.* **104**, 13588-13590 (2007).

902 136 Komabayashi, T., Hirose, K., Sata, N., Ohishi, Y. & Dubrovinsky, L. S. Phase transition in $CaSiO_3$
903 perovskite. *Earth and Planetary Science Letters* **260**, 564-569 (2007).

904 137 Kurashina, T., Hirose, K., Ono, S., Sata, N. & Ohishi, Y. Phase transition in Al-bearing $CaSiO_3$
905 perovskite: implications for seismic discontinuities in the lower mantle. *Phys. Earth Planet. Inter.*
906 **145**, 67-74 (2004).

907 138 Wu, Z. & Wentzcovitch, R. M. Composition versus temperature induced velocity heterogeneities in
908 a pyrolitic lower mantle. *Earth and Planetary Science Letters* **457**, 359-365 (2017).

909 139 Cammarano, F., Marquardt, H., Speziale, S. & Tackley, P. J. Role of iron-spin transition in
910 ferropericlase on seismic interpretation: A broad thermochemical transition in the mid mantle?
911 *Geophysical Research Letters* **37**, L03308 (2010).

912 140 Catalli, K. *et al.* Effects of the Fe^{3+} spin transition on the properties of aluminous perovskite-New
913 insights for lower-mantle seismic heterogeneities. *Earth and Planetary Science Letters* **310**, 293-302
914 (2011).

915 141 Shim, S.-H. *et al.* Stability of ferrous-iron-rich bridgmanite under reducing midmantle conditions.
916   *Proc. Natl. Acad. Sci.* **114**, 6468-6473 (2017).

917 142 Glazyrin, K. *et al.* Magnesium silicate perovskite and effect of iron oxidation state on its bulk sound
918   velocity at the conditions of the lower mantle. *Earth and Planetary Science Letters* **393**, 182-186
919   (2014).

920 143 Fujino, K. *et al.* Spin transition of ferric iron in Al-bearing Mg–perovskite up to 200GPa and its
921   implication for the lower mantle. *Earth and Planetary Science Letters* **317-318**, 407-412 (2012).

922 144 Iitaka, T., Hirose, K., Kawamura, K. & Murakami, M. The elasticity of the $MgSiO_3$ post-perovskite
923   phase in the Earth's lowermost mantle. *Nature* **430**, 442-445 (2004).

924 145 Miyagi, L., Kanitpanyacharoen, W., Kaercher, P., Lee, K. K. M. & Wenk, H.-R. Slip Systems in $MgSiO_3$
925   Post-Perovskite: Implications for D'' Anisotropy. *Science* **329**, 1639-1641 (2010).

926 146 Lin, J.-F., Speziale, S., Mao, Z. & Marquardt, H. Effects of the electronic spin transitions of iron in
927   lower-mantle minerals: implications to deep-mantle geophysics and geochemistry. *Rev. Geophys.*
928   **51**, 244-275 (2013).

929 147 Badro, J. Spin Transitions in Mantle Minerals. *Annual Review of Earth and Planetary Sciences* **42**,
930   231-248 (2014).

931 148 Murakami, M., Hirose, K., Kawamura, K., Sata, N. & Ohishi, Y. Post-perovskite phase transition in
932   $MgSiO_3$. *Science* **304**, 855-858 (2004).

933 149 Tsuchiya, T., Tsuchiya, J., Umemoto, K. & Wentzcovitch, R. M. Phase transition in $MgSiO_3$ perovskite
934   in the earth's lower mantle. *Earth and Planetary Science Letters* **224**, 241-248 (2004).

935 150 Oganov, A. R. & Ono, S. Theoretical and experimental evidence for a post-perovskite phase of
936   $MgSiO_3$ in Earth's D'' layer. *Nature* **430**, 445-448 (2004).

937 151 Wu, Y. *et al.* Elasticity of single-crystal NAL phase at high pressure: A potential source of the seismic
938   anisotropy in the lower mantle. *Journal of Geophysical Research: Solid Earth* **121**, 5696-5707
939   (2016).

940 152 Liu, W., Kung, J., Li, B., Nishiyama, N. & Wang, Y. Elasticity of $(Mg_{0.87}Fe_{0.13})_2SiO_4$ wadsleyite to 12
941   GPa and 1073 K. *Phys. Earth Planet. Inter.* **174**, 98-104 (2009).

942 153 Liu, Z. *et al.* Elastic wave velocity of polycrystalline $Mj_{80}Py_{20}$ garnet to 21 GPa and 2,000 K. *Physics*
943   *and Chemistry of Minerals* **42**, 213-222 (2015).

944 154 Gréaux, S. *et al.* Sound velocities of aluminum-bearing stishovite in the mantle transition zone.
945   *Geophysical Research Letters* **43**, 4239-4246 (2016).

946 155 Sinogeikin, S. V., Bass, J. D. & Katsura, T. Single-crystal elasticity of ringwoodite to high pressures
947   and high temperatures: implications for 520 km seismic discontinuity. *Phys. Earth Planet. Inter.* **136**,
948   41-66 (2003).

949 156 Sinogeikin, S. V. & Bass, J. D. Single-crystal elasticity of MgO at high pressure. *Phys. Rev. B* **59**,
950   R14141 (1999).

951 157 Zha, C.-s., Mao, H.-k. & Hemley, R. J. Elasticity of MgO and a primary pressure scale to 55 GPa. *Proc.*
952   *Natl. Acad. Sci.* **97**, 13494-13499 (2000).

953 158 Jiang, F., Gwanmesia, G. D., Dyuzheva, T. I. & Duffy, T. S. Elasticity of stishovite and acoustic mode
954   softening under high pressure by Brillouin scattering. *Phys. Earth Planet. Inter.* **172**, 235-240 (2009).

955 159 Jacobsen, S. D. & Smyth, J. R. Effect of water on the sound velocities of ringwoodite in the transition
956   zone. in *Earth's deep water cycle, AGU Geoph. Monograph* **168**, 131-145 (2006).

957 160 Li, B. & Liebermann, R. C. Sound velocities of wadsleyite β-$(Mg_{0.88}Fe_{0.12})_2SiO_4$ to 10 GPa. *American*
958   *Mineralogist* **85**, 292-295 (2000).

959 161 Li, B., Liebermann, R. C. & Weidner, D. J. Elastic Moduli of Wadsleyite (beta-Mg_2SiO_4) to 7
960   Gigapascals and 873 Kelvin. *Science* **281**, 675-677 (1998).

961 162 Higo, Y., Inoue, T., Li, B., Irifune, T. & Liebermann, R. C. The effect of iron on the elastic properties
962   of ringwoodite at high pressure. *Phys. Earth Planet. Inter.* **159**, 276-285 (2006).

963 163 Gwanmesia, G. D., Wang, L., Triplett, R. & Liebermann, R. C. Pressure and temperature dependence
964   of the elasticity of pyrope-majorite ($Py_{60}Mj_{40}$ and $Py_{50}Mj_{50}$) garnets solid solution measured by
965   ultrasonic interferometry technique. *Phys. Earth Planet. Inter.* **174**, 105-112 (2009).

966 164 Liu, J., Chen, G., Gwanmesia, G. D. & Liebermann, R. C. Elastic wave velocities of pyrope-majorite
967   garnets ($Py_{62}Mj_{38}$ and $Py_{50} Mj_{50}$) to 9 GPa. *Phys. Earth Planet. Inter.* **120**, 153-163 (2000).

968 165   Irifune, T. *et al.* Sound velocities of majorite garnet and the composition of the mantle transition
969   region. *Nature* **451**, 814-817 (2008).
970 166   Li, B. & Zhang, J. Pressure and temperature dependence of elastic wave velocity of $MgSiO_3$
971   perovskite and the composition of the lower mantle. *Phys. Earth Planet. Inter.* **151**, 143-154 (2005).
972 167   Sinelnikov, Y. D., Chen, G., Neuville, D. R., Vaughan, M. T. & Liebermann, R. C. Ultrasonic Shear
973   Wave Velocities of MgSiO3 Perovskite at 8 GPa and 800 K and Lower Mantle Composition. *Science*
974   **281**, 677-679 (1998).
975 168   Kung, J., Li, B., Weidner, D. J., Zhang, J. & Liebermann, R. C. Elasticity of $(Mg_{0.83}Fe_{0.17})O$
976   ferropericlase at high pressure: ultrasonic measurements in conjunction with X-radiation
977   techniques. *Earth and Planetary Science Letters* **203**, 557-566 (2002).
978 169   Zhou, C., Gréaux, S., Nishiyama, N., Irifune, T. & Higo, Y. Sound velocities measurement on $MgSiO_3$
979   akimotoite at high pressures and high temperatures with simultaneous in situ X-ray diffraction and
980   ultrasonic study. *Phys. Earth Planet. Inter.* **228**, 97-105 (2014).
981